AIRFLOW IN URBAN CANYONS: a comparison of CFD calculated results with values from physical models with reduced scale tested in a wind tunnel.

Luciano Caruggi de Faria [1]

RESUMO

O dimensionamento de estratégias para ventilação natural por pressão de vento para conforto térmico exige uma boa compreensão de vários efeitos climáticos urbanos regionais até os mecanismos do microclima urbano na escala de quadras e edificações. Embora os efeitos de vento impingindo perpendicularmente a blocos isolados sejam conhecidos, poucos estudos abordam ventos paralelos e diagonais a cânions urbanos com várias proporções entre a altura dos blocos e a largura das vias. Este artigo apresenta uma comparação realizada entre resultados calculados com simulações de CFD com valores medidos obtidos com experimentos físicos em um túnel de vento para dois blocos paralelos utilizando várias proporções e para três direções de vento (perpendicular, paralelo e obliquo). Resultados quantitativos para velocidade e direção do vento e coeficientes de pressão e resultados qualitativos para visualização dos efeitos de vento são apresentados e analisados. As simulações de CFD reproduzem as principais características do fluxo de vento ao redor e entre os blocos de forma eficaz. Os resultados também destacam as limitações das simulações de CFD na reprodução de efeitos de desprendimentos e recolocação do fluxo de vento, embora os padrões observados tenham sido identificados para as mesmas configurações de cenários na simulação de CFD e na visualização utilizando bolhas de hélio do túnel de vento. Por outro lado, as simulações CFD identificam velocidade, pressão e turbulência em qualquer direção e região do modelo, permitindo uma avaliação complexa e precisa do problema. Concluindo, a comparação dos resultados calculados com as simulações de CFD com os valores medidos nos experimentos físicos realizados com o túnel de vento apresenta uma consistente correspondência, fornecendo parâmetros adotados nas etapas de pré-processamento, resolução e pós-processamento para futuros modelos computacionais similares.

PALAVRAS-CHAVE: Vento. Canyon urbano. Proporção. Túnel de vento. CFD.

[1] Arquiteto e Urbanista graduado pela FAU-USP (2001) em 2001. Doutor pela Welsh School of Architecture (2012) da Cardiff University, Reino Unido, com diploma convalidado pela USP em 2015. Pesquisador Colaborador no Núcleo de Biomimetismo e Design da Bartlett School of Architecture (BSA) da University College London (UCL), Reino Unido. Pós-doutorado na FAU-USP, com colaboração da School of Architecture, Building and Civil Engineering (SABCE) da Loughborough University, Reino Unido (2023).

ABSTRACT
The design of wind-driven natural ventilation strategies to improve thermal comfort demands good understanding of several regional urban climate effects down to the block microclimate's mechanisms regarding flow effects in and around blockages. While flow patterns impinging perpendicularly on isolated blocks are well-known, less research has been done for channelled parallel and skewed flow in urban canyons with various height-to-width aspect ratios. This paper presents a comparison of calculated results from CFD simulations with measured values from wind tunnel physical experiments for urban canyon-like blockages utilizing several height-to-width aspect ratios and for three (perpendicular, parallel, and at a 45^{o} angle) flow directions. Two identical rectangular bricks were utilized as a simplified approach to investigate the airflow around and in urban canyons, with both quantitative results for wind speed and direction, and pressure coefficients and qualitative results for flow visualization techniques being assessed. The CFD simulations were able to reproduce the main features of the flow around and in the urban canyons effectively. The outputs also highlight the limitations of the CFD in reproducing accurate flow detachments and wake reattachment, although similar airflow patterns were identified for the same set of aspect ratios on both the wind tunnel helium bubble visualization and the CFD airflow visualization by vectors and pathlines. Conversely, CFD simulations identify velocity, pressure and turbulence profiles in any direction and region of the model, allowing complex and accurate assessment of the problem. Concluding, the comparison of the CFD output with the results from the wind tunnel presented a good match, providing parameters adopted on the pre-processing, the solving and the post-processing stages for future computational models.

KEYWORDS: Wind. Urban canyon. Aspect ratio. Wind tunnel. CFD.

INTRODUCTION

Improve the comfort level of people regarding indoor thermal sensation and indoor air quality (IAQ) is both a necessity and a challenge which demands the attention of today's architects and urban planners. To mitigate heat distress and hot/warm thermal sensation, the use of wind-driven natural ventilation (NVw) and buoyancy-driven natural ventilation (NVb) strategies are effective resources to provide thermal comfort and curb energy consumption with HVAC (heat and ventilation air conditioning) systems. Conversely, to ensure that necessary flow rates and air speeds are achieved, architects and building engineers must have a good understanding of several regional urban climate effects down to the block microclimate's mechanisms regarding flow effects around blockages and wind pressure distribution to size openings for both NVw and NVb systems (Givoni 1944, 1998, Melaragno 1986).

In this sense, an approach begins with an understanding of the atmospheric boundary layer (ABL), the region where the 'free atmosphere' characteristics, which is the result of the effect of friction of the surface of the ground on the gradient winds driven by the Coriolis effect in global scale. The ABL comprises the vertical distance from the ground level up to the gradient height, where the wind speed is no longer affected by the unevenness of the ground roughness and is characterized by an increase in average

upward wind velocity that determines the vertical wind profile. Above the Interfacial layer height, the flow tends to stabilize slowly until attaining the wind velocity and direction of the gradient layer. This effect is called the Ekman Spiral and occurs in the Ekman Layer (Figure 1) (MacDonald, 1975; Oke 1978 and 1988; Cook, 1985; Holmes, 2001).

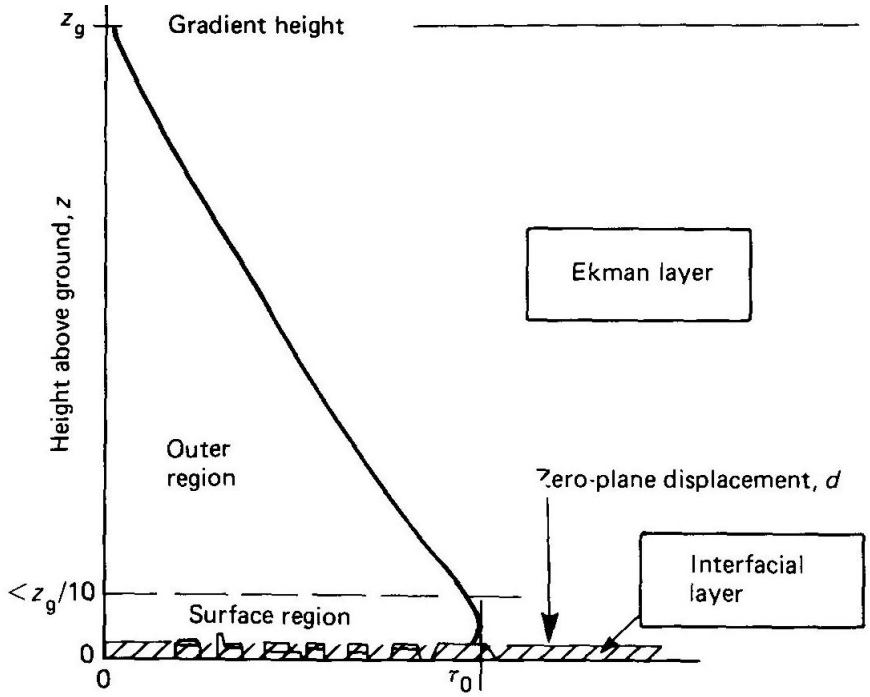

Figure 1: Atmospheric Boundary Layer. Source: Cook (1985, p139).

The interfacial layer extends from ground level up to the so-called either canopy height (Oke 1978 and 1988; Cook, 1985; Givoni 1998), 'obstructed sub-layer' (Kolokotroni and Santamouris 2007) or 'zero plane displacement' (MacDonald, 1975; Cook, 1985; Holmes, 2001), meaning the vertical distance from the ground at which the free airflow momentum is transformed into pressure on windward surfaces. Both the wind profile and the ABL height are determined by the terrain roughness features, although they are also susceptible to influences of small-scale weather systems (Cook, 1985, Holmes, 2001). In a city centre the urban canopy height or zero-plane displacement is related to the average height of the buildings. In this work, the former term will be used in relation to the general description of the urban shape, and the latter will be employed in the specification of the ABL. Holmes (2001) indicates that the zero-plane displacement can be considered as standing at three-quarters of the averaged roof height. Cook (1985) provides a more accurate method for calculating it based on the average height of tall buildings and the plan-area density of the urban site (Equation 1 and Equation 2).

Equation 1: $d = H – [4.3 * Z_o * (1 – a)]$

Where:

1. d: is the zero-plane displacement (m)
2. H: the average height of the buildings (m); and
3. Z_0: the terrain roughness length, a constant of integrations (m); and
4. a: is the plan-area density, calculated as:

Equation 2: $a = Ar / As$

Where:

5. Ar: the total roof area (m^2); and
6. As: the total site area (m^2).

The free and undisturbed airflow above the urban skyline becomes highly turbulent below the urban canopy height (Figure 2). The terrain's roughness determines ABL, and the built geometry and topography induces airflow acceleration or deceleration, creating turbulent and sheltered zones and ultimately defining pressure differences across buildings. This chaotic behaviour can undermine natural ventilation strategies based in openings for wind-driven ventilation and compromise efficiency (Oke, 1978 and 1988). The minimum air changes (ACH) for indoor air quality (IAQ) may be achievable with buoyant-driven ventilation, although rates to mitigate thermal discomfort due to high operative temperatures may be out of reach. To design and size wind-driven natura ventilation strategies for thermal comfort it is necessary to know beforehand, not only the prevailing wind direction and velocity, but how the free airflow is changed locally by the surrounding built-up area to, then, design building's volumetric shape, choose façade materials, size and specify openings, and design the occupant's internal layout, shafts, atriums and any vertical space connection diving or impacting in the natural ventilation strategies for buildings in the urban environment (Masi and Ochoa 2005).

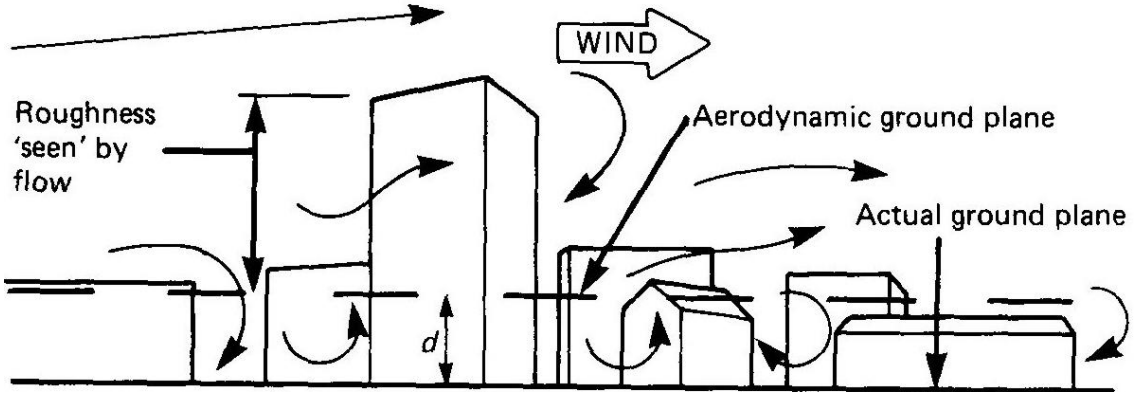

Figure 2: Flow in the interfacial layer. Source: Cook (1985, p139).

When the boundary wind from uniformly flat and constant terrain roughness reaches suburban and urban areas, the boundary develops adopting a profile related to its new characteristic terrain roughness (Figure 3) (Plate and Kiefer, 2001). Although the complexity of the airflow field and the ABL development over urban areas are not just related to two or three terrain roughness types, since the complex tri-dimensional geometry of urban centres allied to the intermittent nature of the airflow and gust speed and direction provides myriad variables, an assortment of mathematical expressions provides models for calculating a two-dimensional mean wind speed profile. These equations take the terrain roughness into consideration in order to dete rmine the variation in profiles (Cook 1985).

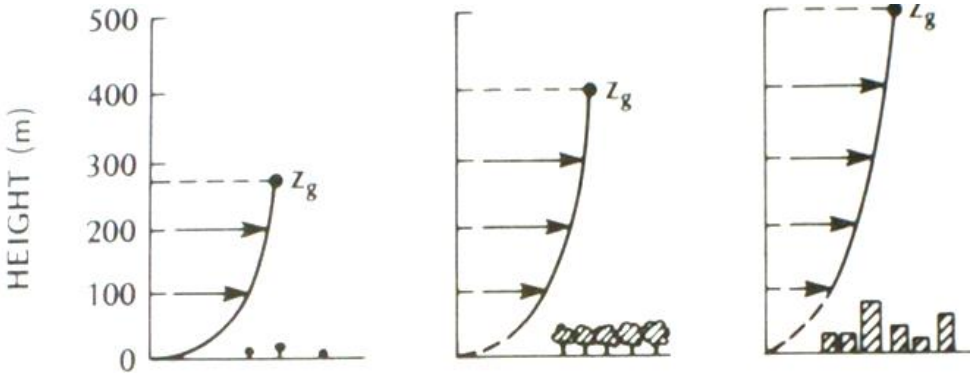

1. (b) (c)

Figure 3: Vertical wind profile for three terrain roughness: (a) open country, (b) woodland or suburban, and (c) city centre. Source: Oke (1978, p45).

The mostly used equations are the 'power law' (Equation 3) and the 'logarithmic law' (Equation 4). When the fully developed ABL for a site encounters a change in the terrain roughness, a velocity and gradient height adjustment takes place from the bottom to the top of the profile until it regains its equilibrium (Holmes, 2001). The fetch is the length term used to describe the radial horizontal dimension from a given terrain with the same roughness characteristics. It specifies terrain roughness changes over distances and their location in the upstream to downstream axis and direction (Table 1) (Cook, 1985).

Equation 3: $$\overline{U}z = \overline{U}_{10}\left[\left(\frac{Z-d}{10}\right)\right]^{a}$$

Where:

1. Uz: is the mean wind speed at Z height (m)
2. U_{10}: the mean wind speed at 10 meters heigh
3. Z: is the height above ground (m)

4. d: is the zero-plane displacement (m); and
5. α: is an exponent, based on the terrain roughness characteristics.

Equation 4:
$$\overline{U}z = \left(\frac{u_*}{k}\right)\ln\left[\left(\frac{Z-d}{Z_0}\right)\right]$$

Where:

6. u_*: is the dimensionless friction velocity
7. k: the dimensionless von Karman's constant =0.4, and 1/k = 2.5; and
8. Z_0: the terrain roughness length, a constant of integrations (m).

Table 1: Terrain roughness parameters 'α':

coastal areas	open terrain 1	open terrain 2	suburban areas 1	suburban areas 2	suburban areas 3	cities 1	cities 2
0.10	0.14	0.16	.21	0.22	0.28	0.33	0.40

Sources: Cook (1985, p184); and Melaragno (1986, p48).

Air moving at a constant velocity and direction exerts a potential pressure denominated static pressure (Ps). When wind, characterized as a laminar air movement parallel to the ground, moves towards a building, it produces varying pressure differences on its frontal, lateral, rear and top surfaces. When it reaches a barrier, the dynamic pressure (Pd) produced is greater than the original potential to windward, and lower to leeward. The dynamic pressure at a specific point of a building's façade is related to the wind velocity and angle of incidence, taking into consideration that both the wind's behaviour and the pressure distribution on a building in the open field and in an urban context are very different. The wind pressure coefficient (Cp) is a function related to the wind velocity at a reference point (V_r), the dynamic pressure on the building's surface (Pd) and the density of the air (ρ_a) that allows the identification of the distribution of wind pressure on a building's surfaces and in the spaces between them (CIBSE Guide A, 2010). Based on the Bernouli principle, the equation for calculating the Cp is (Equation 5) (MacDonald, 1975; Cook, 1985; Holmes, 2001; Awbi, 1991, 2003).

Equation 5: $Cp = Pd / (½\ \rho_a\ V_r^2)$

Where:

Pd: is the dynamic pressure (Pa)

ρ_a: the density of the air (average of 1290g/m^3, varying according to temperature, altitude, and relative humidity); and

V_r: the wind velocity at a reference point (m/s).

Flow patterns around isolated bluff bodies are well-known, and the effects of winds impinging perpendicularly on single blocks have been fully investigated through wind tunnel tests. The results recorded in the literature constitute the basis of knowledge for the calculation of pressure coefficients across buildings and wind loads on structures (Olgyay, 1973; MacDonald 1975; Awbi, 1991 and 2003; Cook 1985; Melaragno, 1986; Holmes 2001). The effects of airflow against bluff bodies are different from those of uniform and variable incident wind profiles (Figure 4). Concisely described, hypothetical orthogonal flow against prismatic sharp-edged shapes, as is the case with most isolated buildings, is related to the impinging boundary wind profile, presenting a front stagnation point (FS) on the windward surface, shear layers in the laterals and flow detachments at the sharp edges, trailing shear layers and turbulent vortex wake of low speed and pressure on the leeward side. While at the first moment the pressure on the windward surface is evenly distributed and has the same value as in the first case, at the second there is a pressure value gradient that corresponds to the variation of the wind velocity with height, and to the consequent kinetic energy. In the first case, as the streamlines flow over the top, there is a pressure gradient on which the bottom centre is the highest point (1.0), the perimeters being the lowest ones (0.4). In the second case the difference in wind velocity produces a region on the windward surface of high pressure, the FS. From the FS point (which is positioned around 2/3rd of the total height) the flow divides into an upward accelerated flow goes over the top roof, and another downward flow that creates a reverse vortex at ground level until reaching the rest in the separation point on the ground, or ground stagnation GS (1/3rd of the total height).

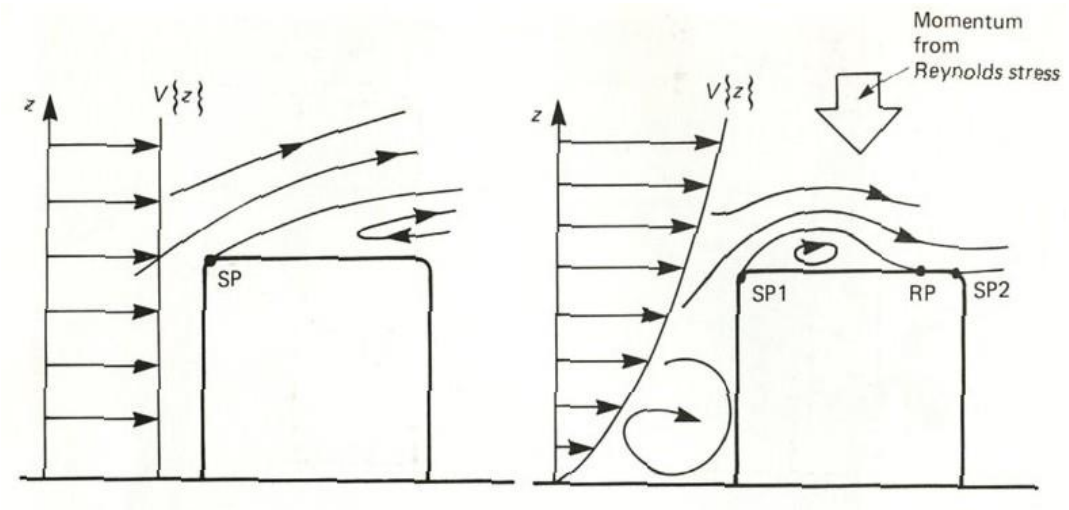

(a)

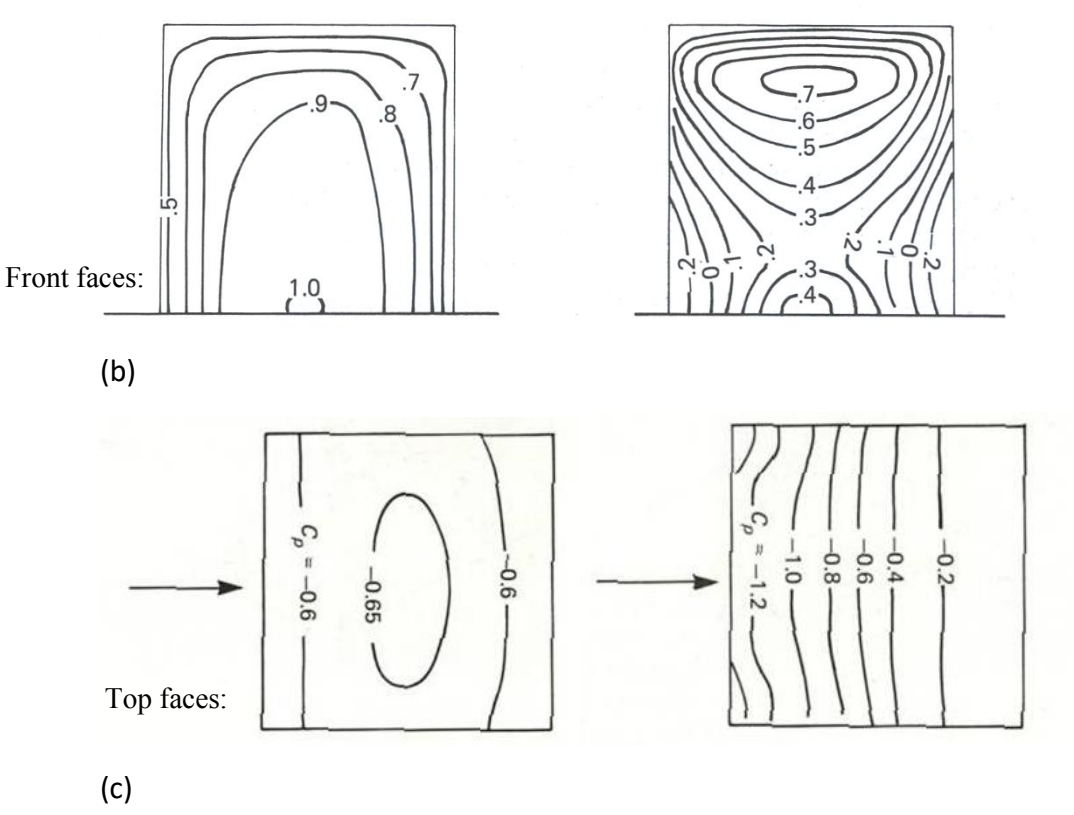

Figure 4: Vertical wind profile (a) and Cp distribution of constant (left) and variable (right) vertical wind profile at the front (b) and top (c) surfaces of a cubic volume. Source: Cook (1985, p. 168).

On tall buildings this downward flow deflects strong high winds to the pedestrian levels, what may incur in pedestrian discomfort and hazard. The flow escaping on each side of the building accelerates near the corners by over 50%, which can also be quite hazardous for pedestrians. In high-rise buildings, i.e., those whose height is greater than three times the width, the pressure distribution pattern presents the greatest distribution of pressure in the centre. The FS point is related to 4/5th of their height and strong downward flows may occur, causing pedestrian hazard or discomfort (Figure 5) (Holmes, 2001). The separation bubble at the top is also different for uniform and boundary layer flows. In the first case, all the flow accumulates upwards, creating a sharp detachment. In the second, only the flow in the last 1/3rd of the height of the building goes upwards. This effect, added to the mean wind kinetic energy, contributes to the flow reattachment downstream on the top surface, occurring at the reattachment point RP. There is also a new detachment from the flow at the leeward edge. Also, part of this downward wind is deflected to each side of the building in a horse-shape form (Figure 6) (Cook 1985; Holmes 2001).

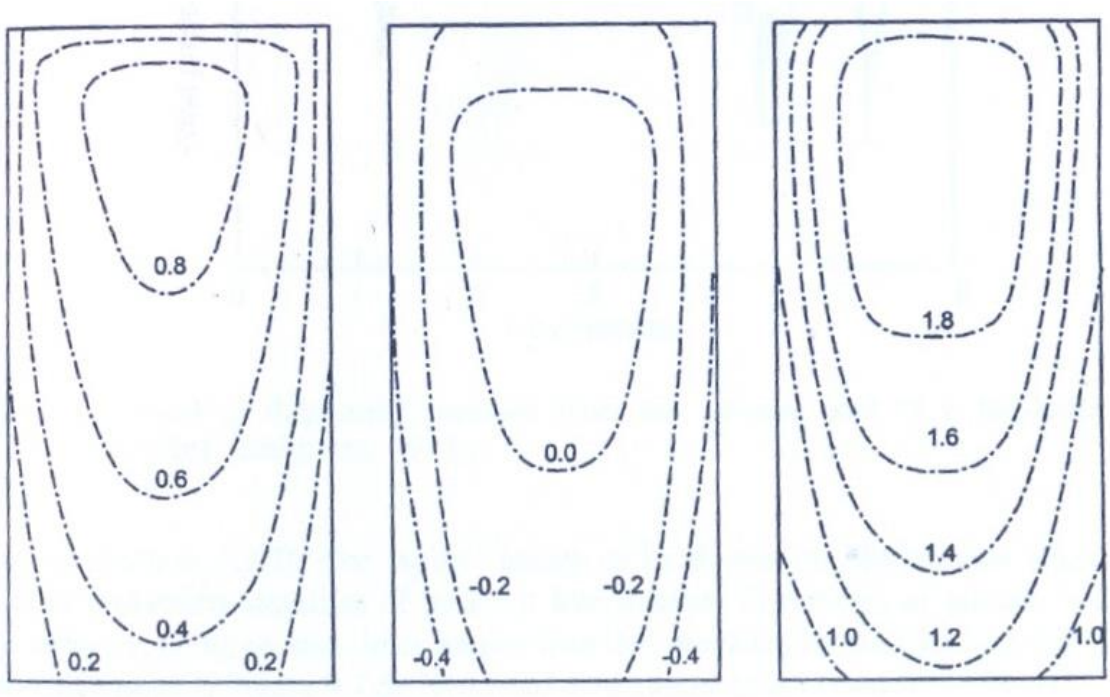

2. (b) (c)

Figure 5: (a) mean, (b) minimum, and (c) maximum Cp distribution of constant vertical wind profile on a high-rise volume. Source: Cheung (1984, in Holmes, 2001, p. 187).

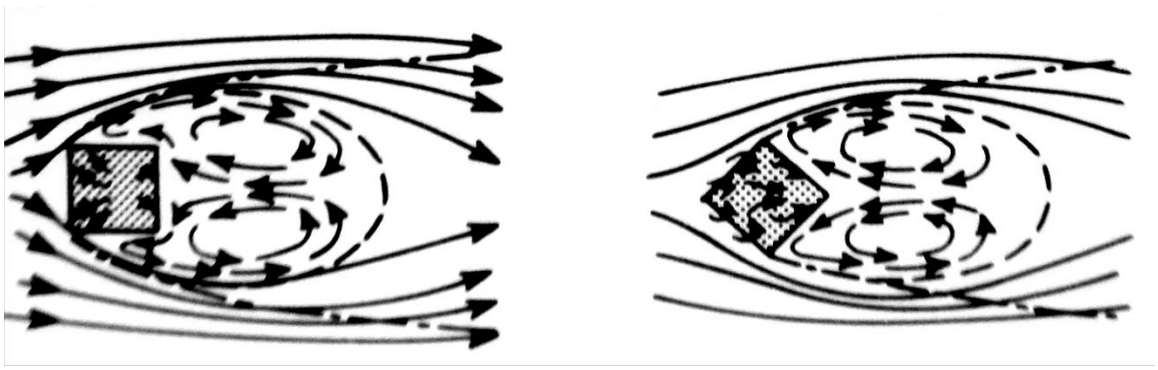

3. (b)

Figure 6: Airflow horse-shoe effect around (a) perpendicular and (b) oblique cubes. Source: Oke (1978, p. 232).

Wakes are formed by the detachment of the flows on sharp edges of a building and have two main components: the near-wake and the far-wake (Figure 7). The near-wake, just beyond the leeward surface, presents a recirculation zone composed of one or more vertical vortexes at its centre and spiral upward eddies on each side. The far-wake is represented by the eventual reattachment of the wake to the main airflow streamlines.

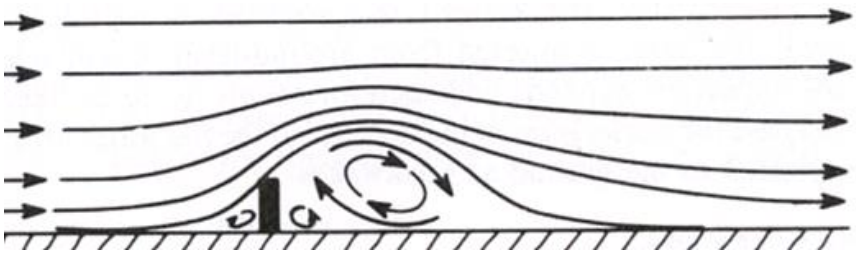

(a)

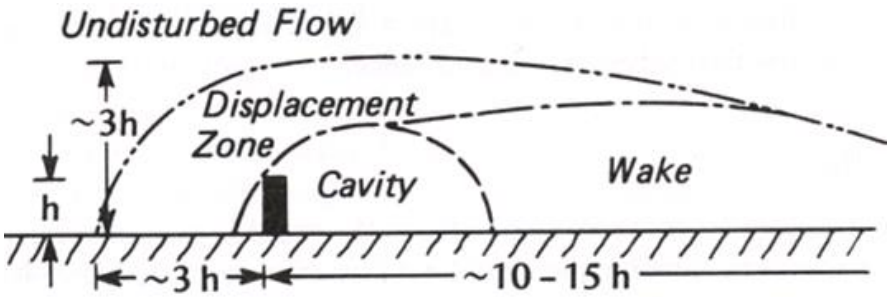

(b)

Figure 7: Schematic views of streamlines (a) and its dimensions (b) around isolated buildings. Source: Oke (1978, p. 212).

Chandra et al (1986) states that, for standard residential neighbourhoods the length of the leeward wake is about four times the ground-to-eave height. In previous studies, Oke (1978) had stated that the total length of the leeward wake to the point at which reattachment flow occurs is from 10 to 15 times the height of isolated high-rise buildings, while the zones of undisturbed flow on the upper and front sides are situated at 02 and 03 times that distance. Experimentation with simple volumes, such as a cube, prism or brick (or an array of cubes such shapes) has allowed direct comparison of CFD simulation data with those of wind tunnel and/ or field measurements. Such comparisons have been used for verifying, calibrating or validating CFD model input information (for instance, domain and boundary layer, turbulence and viscous modes) and other parameters that may affect the accuracy of such simulations of reality.

1. Airflow in urban canyons

The so-called ‘urban canyon’ areas are created by the corridors lying between buildings and are formed by the cavities between the road surface and its flanking buildings, up to roof-top level (Figure 8). This term, initially used for describing narrow continuous streets, came to be applied to wider roads as well, although the term ‘avenue canyons’ can also be found in the literature (Vardoulakis et al., 2003). It is considered that the air volume within an urban canyon plays an active role in the definition of the surrounding urban micro-climate and its interaction with the meso-scale climate (Nakamura and Oke, 1988). Its top also determines the zero-plane displacement in the urban

surroundings. The effects of airflows within urban canyons are usually explored by investigations focusing on the dispersal of air pollution concentration and urban noise, in addition to natural ventilation systems and building energy efficiency.

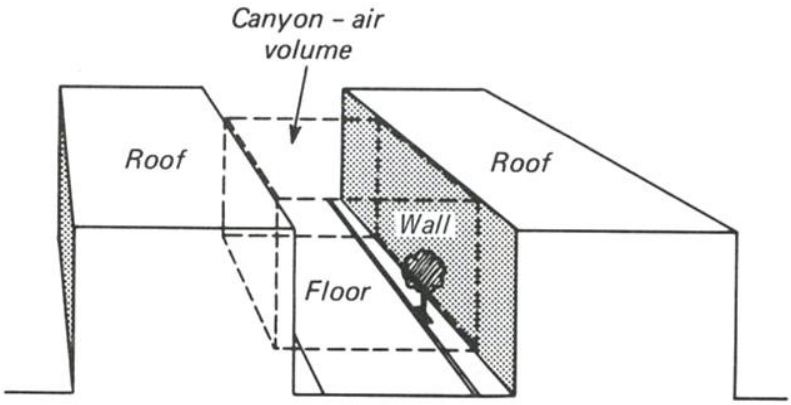

Figure 8: Schematic cross-section of an urban canyon. Source: Oke (1978, p. 250).

Givoni (1976) states that studies with simple canyon shapes based on urban form give an indication of reality such as avoids the interference of other factors in the outcomes, serving as a parameter for other similar, but more complex, urban arrangements. the author stresses that these results are not directly applicable to all real cases. Nakamura and Oke (1988) emphasized that interactions between urban canyons and wind effects were still poorly understood and questioned whether urban climate research had provided sufficient quantitative guidelines such as architects and urban planners could apply when deciding on urban and building geometries. Oke (1988) warns about the impossibility of finding universal solutions, since different climates have specific needs and urban geometry can create conflicts of needs. For instance, solar access and pollution dispersal are improved by open geometry, while densely clustered city centres create shade and shelter and lead to more effective use of urban infrastructure, therefore promoting, on one hand, energy efficiency and, on the other, the concentration of pollution. Successful investigations should include airflow aspects such as skimming flow and channelling effect that can hardly be observed through analytical solutions (Johnson and Hunter, 1998, 1999). Hunter et al. (1991) describes the important role that the urban canyon geometry plays in the near-surface airflow in urban centres. Flow field simulations in urban canyon geometry usually comprise either two or more parallel bricks or an array of rectangular volumes that physically limits the empty space confined in the canyon. The proportionality between the building height (H) and the road width (W) and length (L) identifies the built aspect ratio and the type of volumetric canyon within it. It is expected that the resultant airflow effects below the zero-plane displacement should be connected to variations in these aspect ratios. For instance, the flow field practically does not interact with distant buildings, although the leeward wakes may not develop completely. This is called ‘isolated roughness regime flow’.

Otherwise, for an array of clustered buildings, the leeward wake interacts with the downstream windward bolster and cavity eddies causing secondary flows in the canyon space (Nakamura and Oke, 1988). These urban ratios are given by the relation between the (Equation 6):

Building aspect ratios between the height 'H', the road width 'W' and length 'L', such as: H/W and L/H, which are dimensionless terms

Zero-plane displacement 'd': based on the average height of the buildings and the terrain roughness length (m)

Plan-area density of the urban site 'a' (m^2)

Built-area density of the urban site 'b', defined as follows:

Equation 6: $b = Ab / A$

Where:

2. b: is the built-area density, a dimensionless term
3. Ab: the total built area above ground level, comprising the sum of the floor areas for all storeys (m^2); and
4. As: the total site area (m^2).

A canyon can be considered uniform or regular when its cross-sectional H/W ratio approximates to 1.0, deep or narrow when this ratio increases to 2.0 and wide or shallow when it drops to 0.5. Also, the canyon length L/H ratio is considered short, medium or long for respective ratios of 3.0, 4.5 and 6.0 (Nakamura and Oke, 1988; Vardoulakis et al., 2003). Regarding height, a canyon is considered symmetrical when height is relatively constant and asymmetrical when there is considerable variation in height. Also, windward high-rise buildings are denominated step-up canyons, and the opposite are called step-down. In architectural practice, the terms plan-area and built-area density are related to the building and the plot/ property area. In contrast, here the plot area in fact refers to the urban area surrounding the building(s), comprising the plot area itself but also including the neighbouring plot areas and the surrounding public areas, such as streets, roads, parks and other open spaces. In order to assess the influence of the surrounding built environment in the airflow potential of a given spot, a larger scale is required to verify the urban scale airflow regime.

Wind effects in urban canyons for flows parallel to the canyon's axis create a mean wind component along the canyon's axis with reduced wind speed and possible uplift near the vertical and ground surfaces due to friction (Nakamura and Oke, 1988). In this case the vertical components of velocity tend to be very low and, in the stream-wise direction, if only wind-drive forces are applied. Further, the flow inside the canyon imitates free flow behaviour, but with reduced intensity. For undisturbed winds above the threshold velocity of 2m/s and parallel to the canyon axis, a secondary circulation

flow with a mean wind speed is observed inside it, with low vertical components. The proportional along-canyon wind velocity inside it is linear and related to the angle of incidence of the above-roof airflow. But this coupling is lost for lower speeds, when this proportionality becomes random and scatters (Wedding et al., 1977; Arnfield and Mills, 1994). The same relation was mentioned by Nakamura and Oke (1988) for undisturbed winds from 4 to 5m/s. In addition, for symmetrical canyons, where the mean height of the buildings is the same as the width of the road, or H/W= 1.0, internal velocities are 0.66 to 0.75m/s, when measured internally and externally at heights proportional to 0.06 and 1.20 times the height of the buildings (Santamouris et al., 1999). The same author did not find either this proportionality for deeper canyons (H/W = 2.5) or a clear threshold velocity indicating the existence of coupling, despite statistical analysis's pointing to this correlation. Finally, he concludes that the vertical wind speed at the top of the canyon seems to increase in proportion to the along-canyon free-stream velocity.

Flows perpendicular to the canyon's axis are the most explored within canyon geometry. The effects of normal flow direction have been used as a reference for verifying 2-D and 3-D numerical models for airflow field, turbulence and air pollution dispersion. The following descriptions are based on the studies of Georgakis and Santamouris (2004, 2005) and Cook (1985) for flow effects orthogonal to square canyons (H/W= 1.0). An important aspect observed in this type of flow is the production of vortexes rotating in the mainstream direction below the canopy height and between the two blocks. The vortex occurs as a result of pressure differences between the leeward side of the upstream building (low pressure) and the windward side of the downstream building (high pressure). The pressure difference rises when the free airflow creates an increase in the pressure on the windward surface of the front block and forces a down flow below the frontal stagnation point. The flow separates at the edge of the leeward surface, creating a large wake of low pressure behind the front block. When the detached flow meets the windward surface of the rear block, it tends to be diverted downward, which increases the pressure on the latter block's surface. When, on reaching ground level, the flow turns towards the low-pressure area on the leeward side of the frontal block, it gives rise to a flow across the canyon and in a direction reverse to that of the mainstream. From this point the flow is diverted upwards due to its mass conservation and rises, though with a weaker vertical component. When reaching the top edge, where a strong flow detachment takes place, this flow is deflected into the horizontal wind stream direction again. The vortex created in the canyon space therefore presents wind components near the surfaces but little air movement at its centre. DePaul and Shieh (1986) observe that the vortex centre is situated at 0.75H for symmetrical deep canyons, whereas for deeper canyons (H/W>2) several vortexes of decreasing intensity are created. Chang et al (1971) relate that strong winds orthogonal to a deep canyon create two vortexes inside it: an upper one driven by ambient airflow, and a lower one driven in the opposite direction to that of the circulation above it.

According to the H/W and L/H ratios and the wind velocity, several phases of airflow effect may be noted, including skimming flow for narrow canyons and, as the H/W ratio increases, transition to wake interference and isolated roughness, as several authors have stated (Figure 9) (Oke 1988; Hunter et al., 1991; Sini et al., 1996). Strong winds and/ or narrow canyons cause skimmed flow, which means, that the flow detachment above the zero-plane displacement height prevents airflow entering downwards into the canyon. Wake interference occurs when the upwind block's leeward wake interferes with the downwind recirculation flow. Isolated roughness is observed when blocks are well separated from each other.

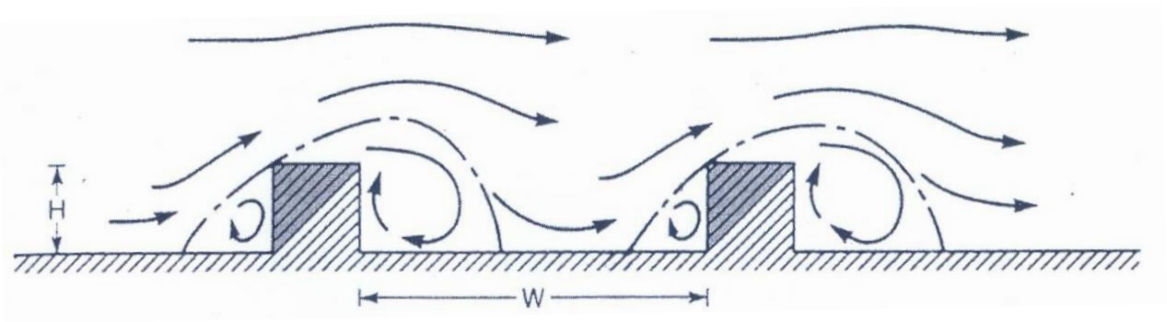

(a)

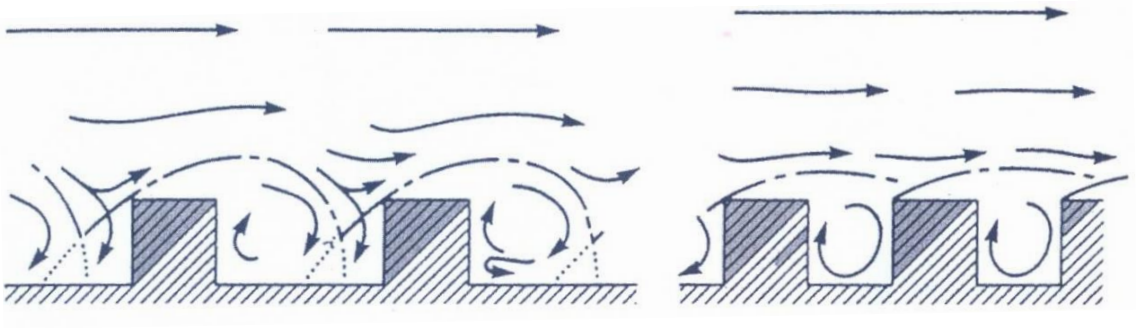

(b) (c)

Figure 9: Flow effects for canyons with diverse H/W aspect ratios: (a) isolated roughness flow; (b) wake interference flow; and (c) skimming flow. Source: Oke (1988, p. 105)

Oke (1988) provides also a graph on which lines distinguish the flow regimes orthogonal to the canyon as skimming, wake interference or isolated roughness flow based on the relationship between H/W and L/H (Figure 10). Hunter et al. (1991), with a view to contrasting these results with numerical models, provide an extensive analysis of anticipated flow regimes in accordance with the L/H and H/W urban aspect ratios. The results for transition from skimming to wake interferences obtained from Hunter et al. agree well with Oke (at H/W~0.7). Also, the change from wake interference to isolated

roughness flow happened at H/W~0.2 for the CFD simulation and at H/W~0.3 for Oke experiment.

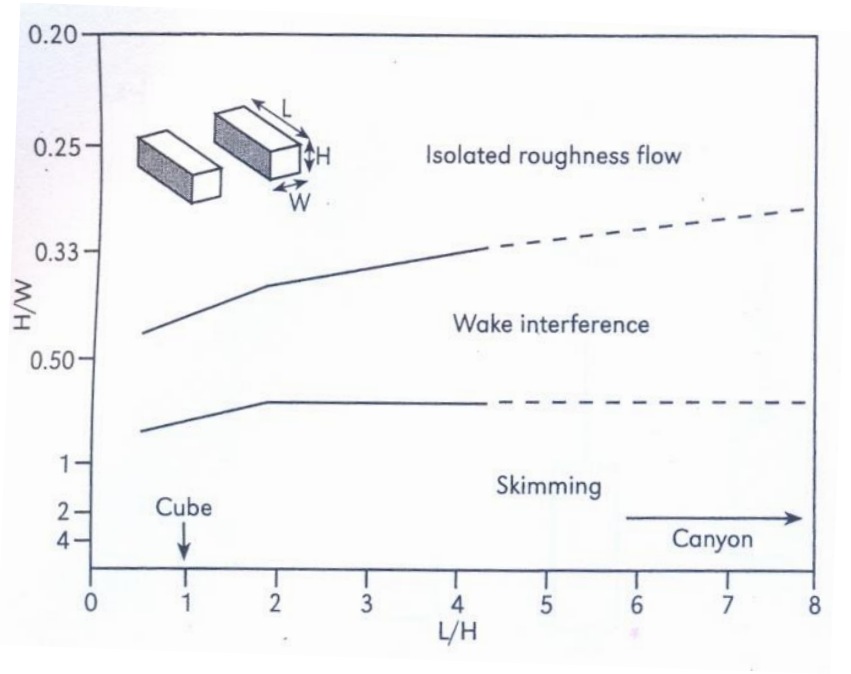

Figure 10: Limits of the airflow regimes for diverse H/W aspect ratios. Source: Oke (1988, p. 105)

Fewer studies have explored airflow in asymmetrical canyons. Hoydysh and Dabberdt (1988) simulated in a wind tunnel the airflow in these canyons. The experiment was based on an array of urban blocks of which the H/W aspect ratio for the first half of the blocks (upwind) was maintained at 1.2 and the ratio for the second half (downwind) varied between 0.5, 1.2 and 2.0. The upwind blocks' L W H dimensions were 60, 20 and 8cm, respectively. A relation is observed between the height of the windward façade of the downstream side of the canyon and the downdraft vertical wind velocity. Flow visualization by tracking bubbles is undertaken. The symmetrical case presented an internal counter-flow vortex escaping from the top after two complete internal rotations. The mean speeds for the descending and ascending flow are 50% and 25% weaker than the reference speed. For the step-up asymmetrical geometry, the internal counter-flow showed a vortex escaping from the bottom after from two to up to five complete internal rotations, and both the speeds for the descending and ascending flow were 50% of the reference speed, due to the increase of the downwind effect on high-rise structures. Also, the step-down asymmetrical canyon presented an airflow reduction of 90% in both sides of the canyon. In contrast to these findings, Arnfield and Mills (1994) state that, for irregular canyons with H/W~ 1.5, vortex circulation speeds are unrelated to the mean wind velocity above the roof level. In addition, step-up asymmetrical canyons show reversed vortexes even with external mean wind speeds

below 2m/s. The highest wind velocities inside the canyon are observed at both the top and bottom, but there is a general decrease in wind velocity in the horizontal component as compared to the airflow above the roof height. Also, 75% of the areas within the canyon present very low air movement.

The effects of skewed flows inside and around urban canyons are less explored, with...

…"existing research on this topic being considerably less than the scientific information for perpendicular and along the canyon flows…" (Georgakis and Santamouris, 2004).

Skewed flows create a spiral corkscrew vortex along the main axis. The mean flow along the canyon axis presents vertical downwards components causing spiral vortexes along the length of the canyon in the upward stream direction but with reduced velocity (Nakamura and Oke, 1988). Also, the transversal component of the flow towards and inside a canyon shape determines the vortex intensity, while the parallel part establishes its length (Yamartino and Wiegang, 1986). For external wind speeds above 1.5m/s, the speed of the vortex increases with the speed of the cross-canyon wind (DePaul, 1986). In symmetrical canyons (H/W=1), the transverse vortex speed inside the canyon is proportional to the above-roof transverse component and independent of the above-roof longitudinal component (Yamartino and Wiegand, 1986).

1. Modelling the airflow in urban canyons

Modelling the airflow in urban areas is necessary to evaluate the potential for wind-driven ventilation, air pollution dispersion, and other environmental issues, and a fundamental tool for essential for the successful design of naturally ventilated buildings and for assessing the built environment and the impact that future construction and may have on the urban microclimate (Plate 1999).

1. Airflow modelling in wind tunnel

Investigations which employ physical models in reduced scale in wind tunnel (WT) chambers have been endorsed by established methodology and are known to be capable of helping to understand the development of the boundary layer and providing insights and measurement data on the airflow field around scale replicas. The WT consists of a physical chamber of limited dimensions in the interior of which wind flows are simulated and are used to test the interaction of airflow with physical models. This piece of equipment is composed of inlet fans, flow straighteners, such as screens, a turbulence generator, an airflow adjustment section, the test section itself and finally an outlet surface (Figure 11). A major input parameter for the wind simulation is the creation of the expected airflow boundary layer in the test section of the chamber, which should correspond to the wind velocity profile attained in real scale areas (Plate, 1999).

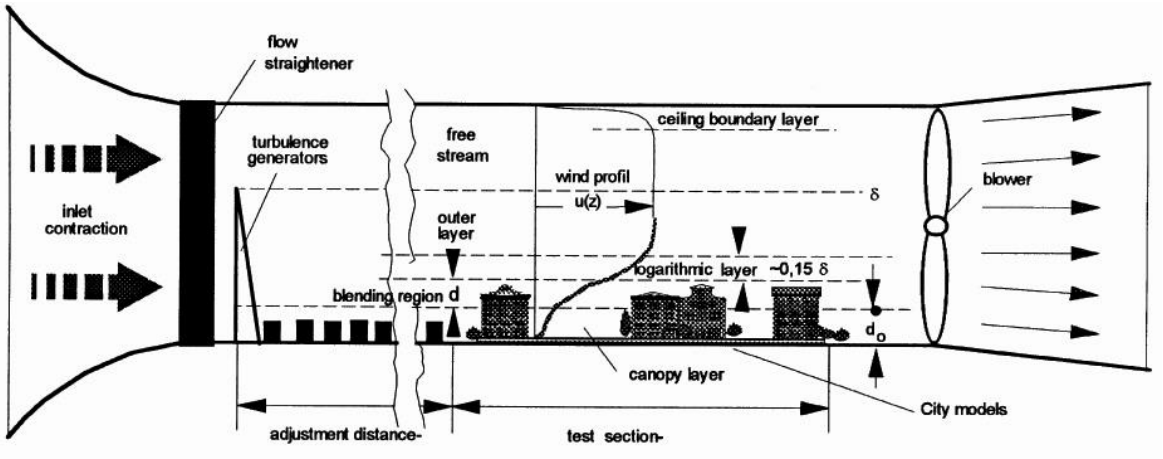

Figure 11: Wind tunnel schematic section. Source: Plate (1999, p. 3.984).

The boundary profile is attained throughout the length of the tunnel by setting the proper ground roughness parameters in the adjustment section. where dragging forces end-up producing shear stress and the vertical stratification of the wind velocity profile equivalent to the real one for the length, width and height of the test section. This proportionality is achieved by the ratio of the wind velocity distribution for a given surface roughness between the natural conditions and the model settings. To obtain consistent results in wind tunnel investigations, the flow effects generated by the model must be proportional to real scale ones. Jensen's scaling laws are usually employed to adapt real atmospheric characteristics for physical scale models in wind tunnels as regards velocity, length, mass and time variations (Armitt and Counihan, 1968; Cook, 1977/ 1978, 1985). Thus, the length and velocities are expressed as ratios, whereas mass variation is related to air density. Other non-dimensional parameters are related to:

The height above ground (typical length variable)

The wind speed coefficient (typical velocity variable)

The roughness number (ground roughness/ structure size)

The density number (inertia of structure / inertia of air)

The Re nº. (inertia of the air / viscous forces); and

The Strouhal nº. for reduced frequency, gravity and elasticity number.

For example, the Reynolds number (Re), which defines the turbulence of the flow, is scaled according to the relationship between the mean airflow velocity (U), the length factor (d) and the kinematic viscosity (n), as follows (Equation 7):

Equation 7: $Re = U*d/n$

Large Reynolds numbers above 5,000 ensure that the flow field is stable through the chamber, suffering no effect of variations in velocity. The valid test height is not the total height of the chamber, since the wind profile varies above the reproduced boundary layer and ultimately is modified by the influence of the ceiling (Plate, 1999).

An advantage of WT is that the complex and almost infinite number of variables existing in the natural environment, which can affect results in field measurements, can be isolated and comprehended on a case-by-case basis (Ahmad et al. 2005). The uncertainties related to the modelling and scaling process are, therefore, plausibly controlled. Such variables may include the mean wind speed and direction, the urban morphology and tissue which affect the topography, for instance, the building geometry and its relationship with street and open spaces (urban aspect ratios), architectonic features (roof shape, canopies, balconies, overhangs), urban equipment (trees, bushes, walls, cars, urban signs), landscaping and topography.

Wind tunnel investigations aim at identifying wind loads and pressure coefficients on surfaces for structural calculation or ventilation rates, air pollution concentration dissipation and wind acceleration at pedestrian level for both comfort and safety purposes (Kastner-Klein and Plate, 1999; Plate, 1999), in addition to flow recirculation, vortexes, detachment and reattachment can be either measured by pulse-wire or laser-doppler anemometers with particle image visualization (PIV) or visualized by bubble-tracking photographic techniques (Summers et al, 1986; Davidson et al, 1996). Ground particle erosion allows the visualization and quantification of wind acceleration and gust speed at ground level (Beranek and Van Koten, 1979; Jones et al., 2004). Local averaged pressures can be measured at individual points or as part of a multi-channel electronic system with several hundred positions from which the pressure fluctuations in the model are transmitted by tubing to a decoder (Holmes, 2001).

Investigations with WT can be performed obtaining accurate results of wind flow velocity and pressure measurements for model scales ranging from 1:250 (building scale) up to 1:500 (block scale). Discrepancies between field measurements and WT simulations of up to 20% are acceptable when the purpose relates to environmental design rather than structural calculation (Summers et al. 1986). Although heat balance is reported to affect the urban airflow, to date most wind tunnels are unable to simulate heat transfer and buoyancy-driven flow.

1. Computational fluid dynamics

Computational fluid dynamics (CDF) software's provide computer-based numeric solutions for the equations governing the flow fluids and offer detailed picture of the airflow and temperature distribution within the assessed space (CIBSE A, 2006). In this way, it is possible to solve problems involving turbulent flows for incompressible fluids

simulated in steady-state and/ or dynamic time-averaged modes and in isothermal or energy balanced solutions. The CFD codes applies the Navier-Stokes equations for solving analytically incompressible Newtonian flows by approximation for energy, mass and momentum for flows, with additional transport equations of turbulent velocity components (Awbi, 1991, 1998a, Elman et al., 2005; Senthooran et al., 2004). Unstructured grid and several options for the boundary conditions allows the modelling of complex shaped walls and input/ output interfaces which enhance the range of flow problems that can be solved by CFD simulations (Vardoulakis et al., 2003). Descriptions and best practice guides in the literature can be found as to steps to be taken in order to achieve good results with CFD simulation. The 'Best Practice Guideline for the CFD Simulation of Flows in the Urban Environment' Cost Action 732 (Franke et al., 2007) provides a 10-step procedure to be followed in the modelling and calculation process to prevent errors and uncertainties in CFD simulations. These steps comprise the definition of target variables; approximation equations; geometrical simplification and specification; computational domain; boundary conditions; initial conditions; computational grid; time step size; numerical round-up; and convergence criteria. Coleman and Stern (1997) have grouped these steps into two main categories, 'errors and uncertainties in modelling the physics' and 'numerical errors and uncertainties', covering many aspects related to verification and validation of CFD modelling. Usual steps involved in CFD simulation are suggested during the pre-processing, the solving, and the post-processing of problems (Vardoulakis et al, 2003).

The parameters of interest related to microscale meteorological airflow investigations that suit the urban microclimate assessment provided in the post-processing are:

Air velocity (magnitude, X, Y, Z, relative, etc)

Pressure (static, Cp, dynamic, absolute, total and relative)

Turbulence (intensity, kinetic energy, dissipation rate, viscosity, etc)

Temperature (static, total, enthalpy, surface, energy, etc); and

Concentration (mass, diffusion, relative humidity, etc).

Turbulent flows of small scale and high frequency make the calculation of momentum, energy and concentration transport difficult. Here a comparison between how both the k-e and the LES models tackle this issue and when to use each one of them is presented. Regarding the choice of turbulence models, these are sub-divided into several categories, and must be selected according to what is expected as a result based on the characteristics of the turbulence for the problem imposed (Sini et al., 1996; Dixon et al., 2006). The most used for airflow modelling in the external environment are:

4. Standard k-e model, also defined as Reynolds-averaged Navier-Stokes (RANS)
5. Renormalization-group (RNG) k-e
6. Realizable k-e; and

7. Large Eddy Simulation (LES).

Mesh quality is related to both the convergence time and the accuracy of results. The mesh should be able to capture the important features of the blocked geometry. Sharp edges and constrained gaps in the domain with coarse cells should be avoided, since the resulting airflow will not be realistic. Initial mesh quality and space discretization are established by the number of node points, faces and cells (density and clustering) and the type of mesh in the fluid domain. Further improvement can be achieved by grid adaption in specific regions of the domain. The nature of the problem will influence its resolution, since turbulent flows, shear areas and mixing areas are more susceptible to the dependence on grid 'smoothness' (i.e., maximum aspect ratio between adjacent cells of 1:2 or 1:3, though no larger than 1:5) and 'skewness' (asymmetry and angularity between cells) than laminar flows. Taking hexagonal cubic cells as an example, it is important to highlight that, if the aspect ratio between cells is 1:2 or 1:3, the volume ratio between them will be 1:8 or 1:27, respectively. An aspect ratio of 1:2 for tetrahedral cells will result in a volume ratio of approximately 1:7. It is assumed by the research community that coarse mesh will impact the quality of the results more than other factors, such as the turbulence model or the boundary input. The equations are solved for each cell of the domain, which exchanges values with the surrounding ones. A complete loop of calculation occurs when a solution is given for each cell of the finite-volume, which characterizes one round of iteration. This round repeat either until the predetermined number of iterations is completed or the calculation meets the solution criteria adopted. Convergence is achieved once all discrete conservation equations are attained in the domain to a designated tolerance: the mass, momentum, and energy are in balance and the solution does not improve significantly despite further iterations. Verification and validation using CFD models are necessary to confirm confidence in results related to the assessment of airflow patterns in the urban environment, and they are usually obtained by comparing the outcomes with those of WT or field measurement (FM) research (CIBSE A, 2006), with several examples described in literature (Caretto et al. 1972; Summers et al. 1986; Yamartino and Wiegand 1986; Hunter et al. 1991; Sini et al. 1996; Johnson and Hunter 1998; 1999; Meroney et al. 1999; Jeong and Andrews 2002).

About this paper

This paper presents a comparison of calculated results from CFD simulations with measured values from wind tunnel physical experiments for urban canyon-like blockages utilizing several height-to-width aspect ratios and for three (perpendicular, parallel, and skewed) flow directions. This paper is divided into four chapters: 1. Introduction, presents the problematic addressed and the literature review on the subject investigated; 2. Methodology, presents details of how each stage was structured to meet the established objectives; 3. Results, comprises the critical analysis of the results presented for the stages that make up the analyses; and 4. Conclusions, highlighting the main findings of this research.

Methodology

The methodology adopted for this research for assessing the airflow field in urban canyons comprised the comparison of laboratory scale-model tests in a boundary layer wind tunnel (WT) with computational fluid dynamics (CFD) models.

Designing wind-driven natural ventilation (NVw) systems for indoor environment and to perform at satisfactory levels involves the previous analysis of the airflow field in the external environment. This is necessary to determine whether the site offers the potential for the use of this technique. The potential is subject to urban environment shape and the airflow field below urban canopy height. The urban shape can be described in terms of several physical dimensions, areas and volumes that define aspect ratios, such as building height to road width (H/W) or length (L/H), plan-area density (a= A_{roof}/ A_{urb}) and built area density (b= A_{built}/ A_{urb}). The relationship between the resultant airflow field and the urban aspect ratios is the basis of the investigation on an urban scale. In this research two identical rectangular bricks were utilized as a simplified approach to investigate the airflow around and in urban canyons. To assist the investigation, both quantitative and qualitative information are necessary. While the results of wind speed and direction, and pressure coefficients provide quantitative numerical information, flow visualization techniques allow a qualitative understanding of airflow behaviour around buildings and other physical barriers. The combined analysis of the outcomes of these techniques compared to the urban aspect ratios may then allow this research to propose a scale to represent the potential for natural ventilation in existing urban areas. Both the quantitative and qualitative data were obtained by experimentation with scaled physical models in a boundary layer WT; and with CFD calculations. CFD and WT outputs are compared to ensure the quality and reliability of the numerical simulations in reproducing airflow in external urban environments. The comparisons between the results are aimed at spotting the accuracy and consistency achieved in the CFD simulations undertaken for three wind directions: perpendicular (90˚), parallel (0˚), and oblique (45˚) flows towards the two bricks. Not all the possible combinations between the aspect ratios and the airflow directions were undertaken by both the wind tunnel and the CFD techniques. Good results and comparisons were achieved with the combinations given in Table 2. Further simulations would either produce redundant results or be too time-consuming. Moreover, some of these combinations appeared to be impracticable for several selected methods of simulation and adopted output post-processing. For instance, the wind tunnel airflow visualization with helium bubbles, performed well for perpendicular settings only, since the position of the acrylic brick for parallel and oblique winds produced too much glare and did not allow the analysis of the resultant flow. For instance, a set of parallel bricks was placed orthogonally to the airflow direction.

Table 2: methods of simulation and output post-processing technique employed for the several combinations of aspect ratio and position vis-à-vis main airflow.

H/W ratio →		0.50	0.66	1.00	2.00
↓ Method / Output ↓		prevailing wind direction			
Wind Tunnel	bubble visualization	90˚	90˚	90˚	90˚
CFD	vectors & pathlines	90˚	90˚	0˚ 45˚ 90˚	90˚
Wind Tunnel	contour plots & data	0˚ 45˚ 90˚	0˚ 45˚ 90˚	0˚ 45˚ 90˚	0˚ 45˚ 90˚
CFD	contour plots & data	90˚	90˚	0˚ 45˚ 90˚	90˚

The wind tunnel (WT) experiments

Flow experiments with physical models at reduced scale were performed in the wind tunnel facility at the Welsh School of Architecture (WSA), Cardiff University (Figure 12). This adiabatic ABL WT allows the investigation of scaled flow around physical models to assess and measure wind speed and turbulence, pressure and airflow visualization techniques, such as ground erosion and air bubble tracking. It has a total length of twelve meters and is powered by two 13hp fans providing a maximum speed of 11m/s at 1,100 rotations per minute (RPM) (Fig.12a). The imposed flow is straightened, and the required scaled ABL achieved over an adjustment area of six meters in length composed of several different obstacles and blades, including 'Lego Duplo' blocks on the bottom surface for various terrain roughness features. The lower levels of the atmospheric wind profile are obtained at the modelling section, a rectangular working area in the physical chamber of 2.0m length and side and 1.6m height. The physical models are deployed on a round table of 1.80 m diameter, which allows the exploration of the wind's incidence at any angle. The test area of the chamber with no interference of the side and top surfaces on the experiment's results should have a diameter of 1.50m and a height of 1.00m, and the ABL reproduced is recommended for physical model scales ranging from 1:200 to a maximum of 1:400. The wind profile produced in the modelling section was previously checked by measuring the mean wind speed with Dantec hot-wire and laser doppler anemometry equipment at two points at the same instant of time in order to permit comparison of the data for inlet wind speed of 10m/s created with two fans

working at a constant 900 RPM. This experiment was carried out by this researcher with the support and assistance of two staff teams from the CRiBE/ WSA2.

Figure 12: Wind tunnel facility at the WSA (a) and the chamber and probes used for ABL measurements (b).

The Lego blocks in the adjustment area were set up to reproduce a terrain roughness of category 05, reproducing urban areas with most buildings of four or more storeys and a zero-plane displacement height corresponding to three-quarters of the average building height of 25 meters, and 30-50% of plan-area urban density (Fig.12b). The resulting wind profile presents a satisfactory measure of agreement with those based on the terrain roughness characteristics of urban areas (Equation 8) (Figure 13). The wind pressure coefficient (Cp) is a dimensionless number that can be either positive, for windward forcing pressure, or negative, for leeward suction pressure. The wind pressure coefficient difference (ΔCp) at any two points is employed to determine the airflow ratios for natural wind driven ventilation systems in the internal environment. The WSA WT equipment for measuring Cp (Furness low pressure transducers with Scani-valve scanners) allows the measurement of the mean pressure coefficient only, since peak values are not captured. For this research, each of the mean Cp values considered was the average calculated from at least five successive measurements for each point to avoid the interference of any real random turbulence inside the chamber. As the critical literature review has highlighted, a difference of up to 20% on the results and a wind Cp range of ±0.10 may be acceptable from WT results when the focus of the investigations is not structural calculation.

2 Special thanks are due to both the WSA Senior Lecturer Don K. Alexander and the Research Assistant Dylan Dixon, for calibrating the wind tunnel at this stage of the investigation.

Equation 8: Equation for the scaled Atmospheric Boundary Layer

$$\frac{Z_{point}}{Z_{reference}} = \frac{\overline{U}_{point}}{\overline{U}_{reference}}$$

Source: Cook (1985).

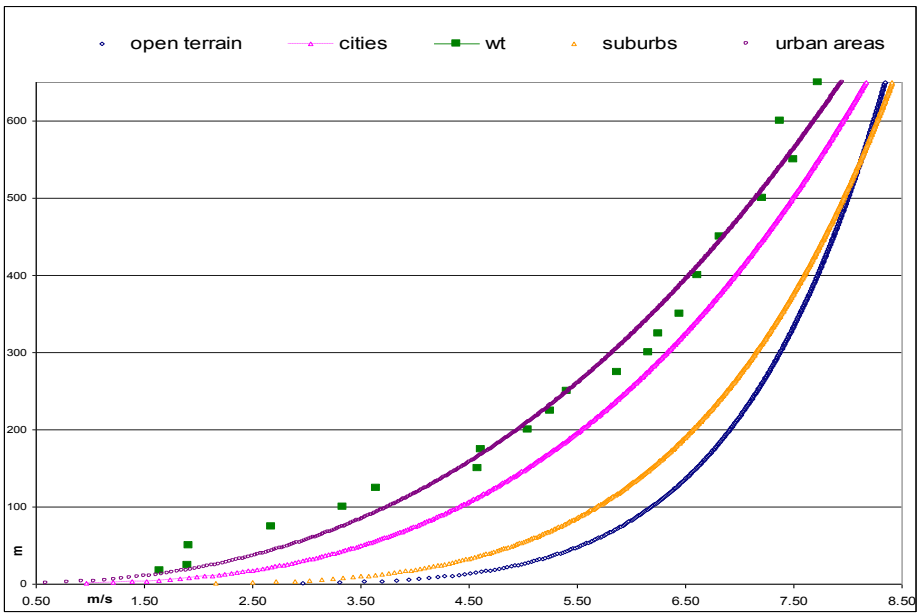

Figure 13: U_{ref} ratios and ABL attained in the wind tunnel compared to those resulting from diverse terrain roughness factors. Source: WSA/ CRiBE.

A total of 164 pressure taps were included in three sides of the acrylic brick of 20x40x10 cm (height, length, and width), representing an urban block of 50x100x25 m scaled at 1/250 (Figure 14). This experiment was set up varying the H/W aspect ratio between the blocks and the position about the airflow inlet, denominated as follows: parallel (0˚), oblique (45˚), and perpendicular (90˚) flows. The wind CP at any point of the model was calculated by the ratio between the pressure at each of the measured points (P_{point}) and a free-stream reference pressure ($P_{reference}$). Both the point and the reference pressures are measured and logged instantaneously (Equation 9). Hence, due to the scaling laws, the Cp is comparable to those obtained in real building envelopes through field measurements. It is further utilized for calculating mean pressures for any given wind speed (Equation 10). Eventually, pressure coefficient contour plots and scattered plot matrices were generated by using the software Axum 6.0 for Windows. The software allows a visual analysis of the Cp distribution and a straightforward qualitative comparison between the wind tunnel measurements and the CFD results.

Equation 9: The wind Cp equation for WT outputs (Cook 1985; Holmes 2001).

$$Cp_{point} = \frac{P_{point}}{P_{reference}}$$

Equation 10: Bernoulli pressure equation (Cook 1985).

$$P_{envelope} = \frac{1}{2} \rho Cp U^2_{ref}$$

The flow around a translucent model was observed using the helium bubble flow visualization technique, which consists of the injection of a controlled number and size of helium bubbles in a dark chamber that are picked out by a beam of light whilst in movement, carried along by the airflow. The capture of images by both a digital photographic and film camera allows later qualitative analysis of flow detachments, vortexes and other airflow effects.

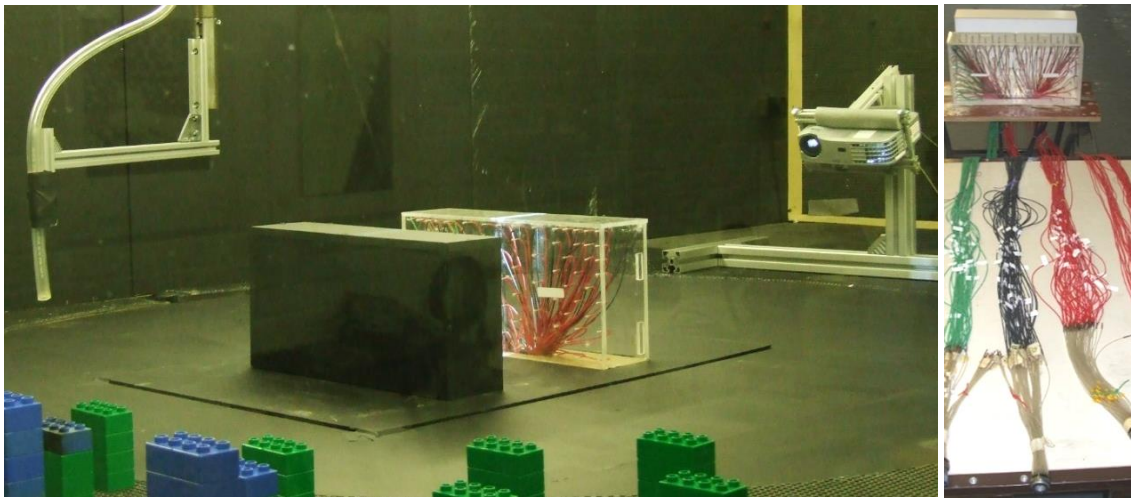

8. (b)

Figure 14: Set-up of one of the physical models for the airflow visualization (a) and detail of the pressure taps placed in the acrylic brick (b).

The computational fluid dynamics (CFD) simulations

Calibration, verification and validation of the parameters used in the CFD simulations were attained by calculating the flow field around two parallel rectangular bricks and contrasting the results with those of the wind tunnel physical model. A total of seventy-five CFD calculations were made to provide information for comparison of measured values from the WT tests and to investigate scenarios not reproduced with the physical models. The CFD programme used was a research version of the ANSYS FLUENT and the 3D models were built and meshed in the Gambit software. The calculations were run in

a Linux based computer. Several guidelines described in the introduction were adopted for the pre-processing, solving and post-processing stages to ensure consistency in the modelling for all CFD calculations undertaken.

The proportion of fluid to blocked cells inside the total domain was kept at 3.0%. The upstream boundary was set at 'velocity inlet' and it was through this surface that the ABL was launched into the model. A velocity magnitude was related to each vertical strap on this surface and the resulting airflow normal to the boundary reproduced the type of ABL calculated by a vertical profile for a given terrain roughness. The sequence of vertical velocity magnitude development that determines the ABL velocity inlet for the CFD simulations is demonstrated in Figure 15.

The boundary types used were velocity inlet; interface; non-slip walls; symmetry; and outflow boundaries. For the intention of contrast the calculated output with the wind tunnel results, both the size of the chamber and the definition of the walls were kept as similar as possible to those of the physical chamber. In this case, lateral and top boundaries were considered as walls. The total domain sub-division into four or five nested volumes was adopted on in the CFD models. The domains were classified as: inlet, centre, outlet, and one or two top zones. This allowed different cell treatment for each zone and, therefore, ensured mesh accuracy where necessary without compromising the final outcomes or the calculation time. Also, the total length and volume adopted for these cushion domains have proved to be sufficient to allow full development of the airflow-field without interfering in the flow patterns in the target area. The nested domains were connected by standard interface boundaries. Neither periodic nor coupled interface was considered in these simulations.

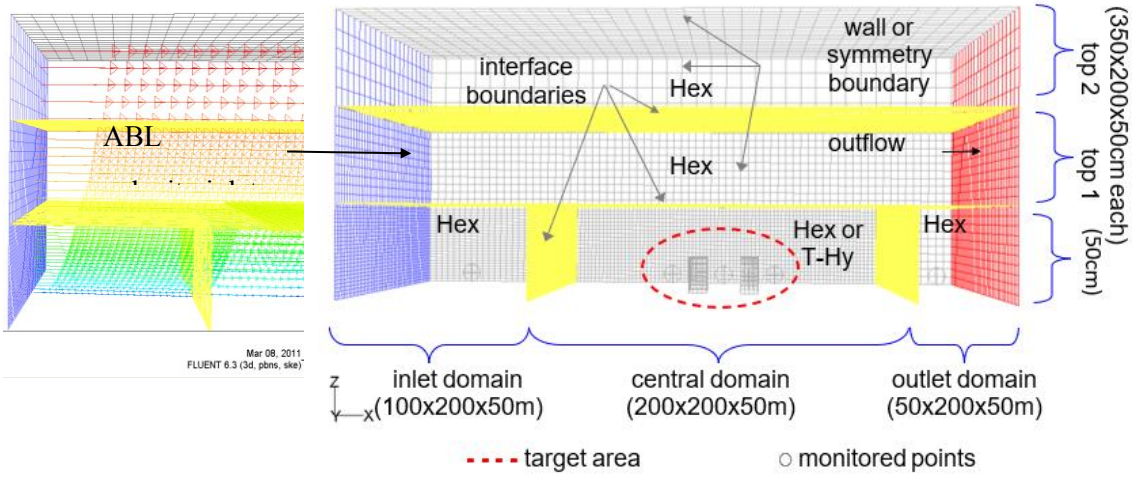

9. (b)

Figure 15: Schematic chart for the ABL wind profile log-law development applied in the investigations and as input in the CFD models (a) and domain size and description of the boundaries for the two-brick CFD model (H/W=1.0; 90o) (b).

The rectangular shape of the several nested volumes that form the domain, and the absence of blocked cells allowed the use of hexagonal structured cells through these domains (Figure 16). Tetrahedral cells creating pyramidal and wedge-shaped volumes were used in the target area mostly in the meshing of non-orthogonal (Fig.16a), skewed and curved blocked shapes, which occurred due to the shape's complexity or the rotation of the model in order to simulate 45º oblique flow (Fig.16b). Grids and meshes were applied in Gambit in the following order: to the surfaces of the target blocked cells, other blocked cells, ground boundary, inlet boundary, outflow boundary, lateral and top boundaries; and, only then, was the mesh volume applied to the target's central domain, the inlet domain, the outlet domain, and the several top domains, respectively. Since the CFD models in this investigation were intended to reproduce reality on an urban scale, one drawing unit was considered equivalent to one meter. A cell of 1x1x1 d.u. has, therefore, a volume of $1.0m^3$. Further mesh improvement in the target area was undertaken on Fluent by region adaption, on which an input coordinate limits the hexagonal volume constraint to be refined. By using a maximum level of mesh refinement equal to one and setting a minimum cell volume of $0.125m^3$, an aspect ratio of 1:2 between adjacent cells was achieved. The horizontal resolution obtained for the grid was a minimum of 20 cells between blockages and canyons in the target area and 10 cells between solid bodies elsewhere in the model. The total number of cells in the CFD models used ranged from 300 thousand cells for the two-brick simulations to 1.0 million cells for the complex urban geometry in the case studies and 1.5 million cells for the urban prototype models. Accuracy in the results has proved to be satisfactorily achieved with the mesh refinement of this scale and order of magnitude.

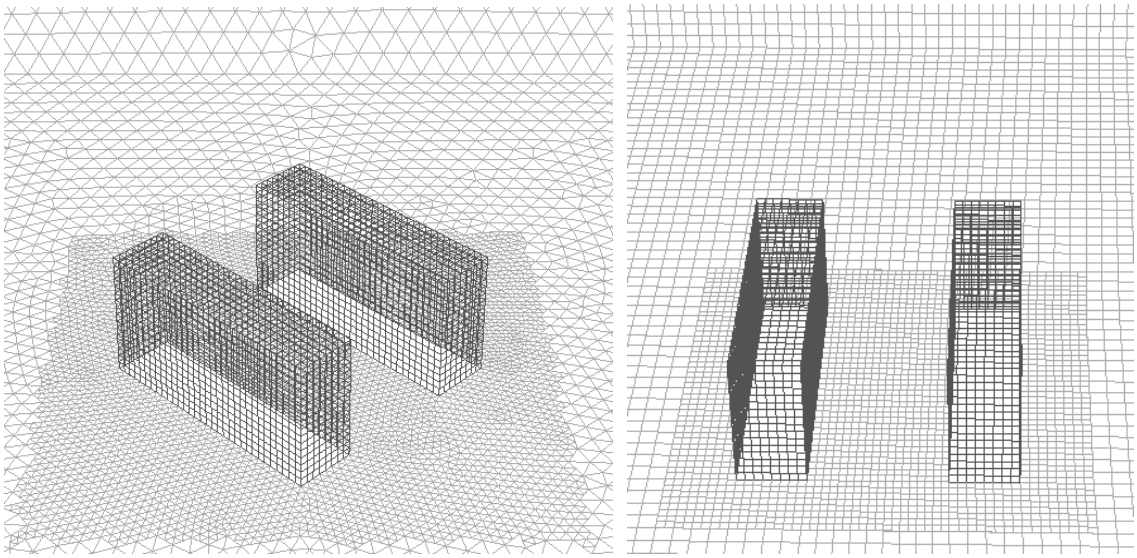

10. (b)

Figure 16: Region mesh adaption undertaken for hexagonal and tetrahedral cells.

The turbulent viscosity model adopted for all the CFD simulations was the k-e RANS standard. In addition, some experiment was carried-out for the purpose of contrasting the results of the standard viscous model used with the k-e RNG; the k-e Realizable; and the LES outputs (de Faria, 2008). The solution controls and under-relaxation factors adopted were kept like the default values. The convergence criterion for the continuity, velocity, turbulence and viscosity equations was achieved after the drop of four orders of magnitude for all the residual plot criteria. In addition to the default solution residual plot, the airflow velocity, turbulence and static pressure were monitored at three or five points strategically positioned throughout the domain, with stability reached for ranges of less than 0.10 unit on the convergence history plot. The Cp variation on some of the blocked target surfaces was monitored with results being considered stable for result ranges inferior to 0.05.

To analyse qualitatively the CFD results, contour plots were used for contrasting Cp results on the block surfaces from the CFD simulations with those from the WT experiment, and velocity magnitude pathlines were used for visualizing the airflow field through the blockages. The quantitative data from the CFD output were extracted either from lines or from surfaces, providing data for velocity (magnitude, 'x', 'y', or 'z' vectors), Cp values, pressure (static, dynamic, relative, total, absolute, Cp) and turbulence (TKE, intensity, dissipation, viscosity). Horizontal lines were strategically positioned either across or alongside the targeted windward and leeward surfaces, and vertical lines were placed either at 0.50m from these surfaces or exactly in between the blocks, from the ground to 200m height (Figure 17). Data was exported as comma delimited in ASCII format and exported to Excel software to build graphs.

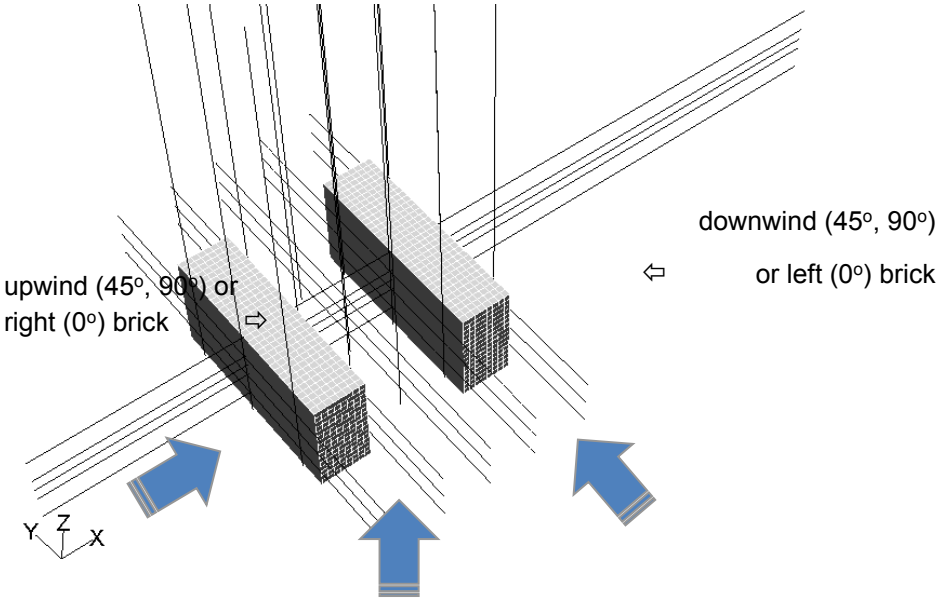

Figure 17: Top view of a set of bricks with the vertical and horizontal lines accessed.

Calculated results from CFD and measured values from WT

Here are presented and discussed the comparison of calculated results from CFD simulations with the measured values for wind tunnel (WT) tests. In total, the scenarios comprised four different H/W aspect ratios (2.00, 1.00, 0.66 and 0.50) and three wind directions (90˚, 45˚ and 0˚). Conversely, due to the limitations of maximum number of words, the results shown here display some scenarios. All results can be accessed in an appendix document available via the GD link: https://drive.google.com/drive/folders/1D-dsJyPTY2bZhD6AIaeHy2OeztA8CKKd?usp=sharing

The results displayed here are shown first for contour plots and graphs depicting the pressure coefficient (Cp) results on these surfaces. Then, velocity vectors and pathlines, from CFD, and airflow bubble still images, from WT, are presented for the visualization of flow effects. Finally, the vertical wind profile from the CFD simulations is shown for 15 vertical lines strategically positioned.

Pressure Coefficient (Cp) results

Here the Cp results are presented. The Cp CFD contour plots are related to a reference velocity value of 2.35m/s, which correspond to the airflow velocity at 10m above the zero-plane displacement.

1. Bricks perpendicular to the airflow (at 90˚)

The contour plots for the upwind brick windward face follows the same patterns on both wind tunnel and CFD results. On the other hand, the range of values is up to 0.30 greater on the later one. The numerical calculation seems to over predict the pressure on the leeward surface, which could be explained by the nature of the k-e model adopted and its limitation on calculating flow recirculation and leeward wakes. In the following figures (Figure 18 to Figure 20) Cp results on the rear side of the front brick will be presented for a range of H/W aspect ratios. This side consists of the leeward face in a canyon for orthogonal winds. Good similarity in the contour plots was found for each of these pairs. Regarding the range of the results, the wind tunnel numbers are constantly lower than the CFD ones presenting a difference between 0.10 and 0.15. Further on, Cp results from the windward side of the downwind brick are shown for the same range of H/W aspect ratios. Once more similar contour plots can be observed between the wind tunnel and the CFD outputs. Regarding the range of the results, it was found that the Cp values from the top height were very close, while the ones near the ground from the WT were up to 0.10 lower than the CFD ones.

When comparing the impact of the aspect ratio has on the Cp values, it was found that for the bricks with a narrow gap in between (H/W = 2.00) results were quite lower than

the others with a square (H/W=1.00), or wide (H/W=0.66 to 0.50) gap, which may be an indicative of the occurrence of skimming flow. Moreover, the results found for the ratios of 1.0, 0.66 and 0.5 were quite similar, although the contour plot shape for the wider ones present in both methods of simulation a distortion towards one side, which might indicate wake interference flow.

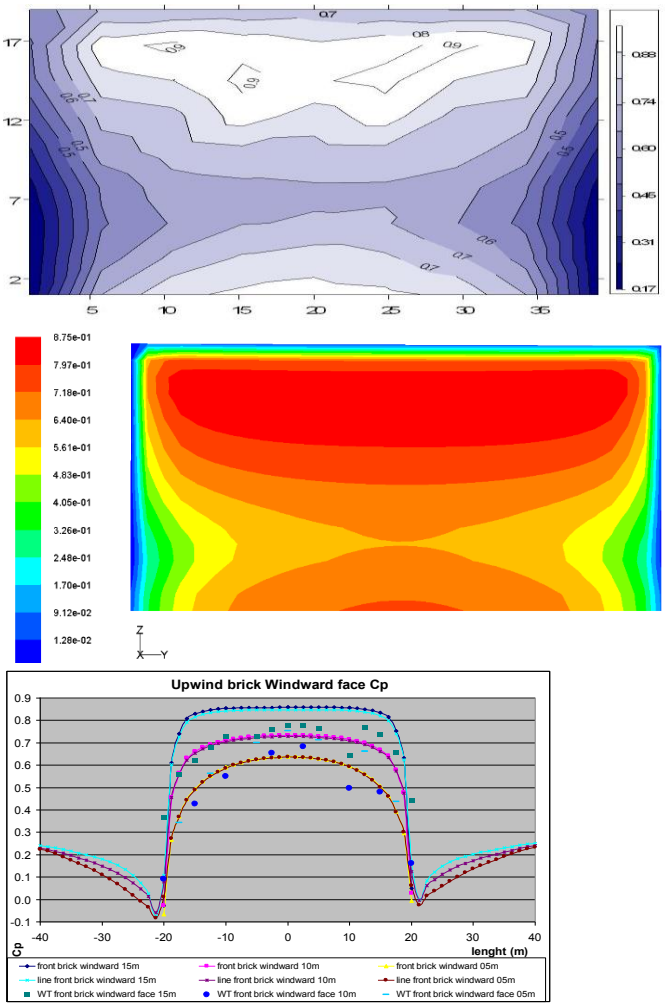

Figure 18: WT (top), CFD (middle) and Cp's contours plot and graphic (bottom) for the upwind brick windward face at 90˚ (H/W=1.0).

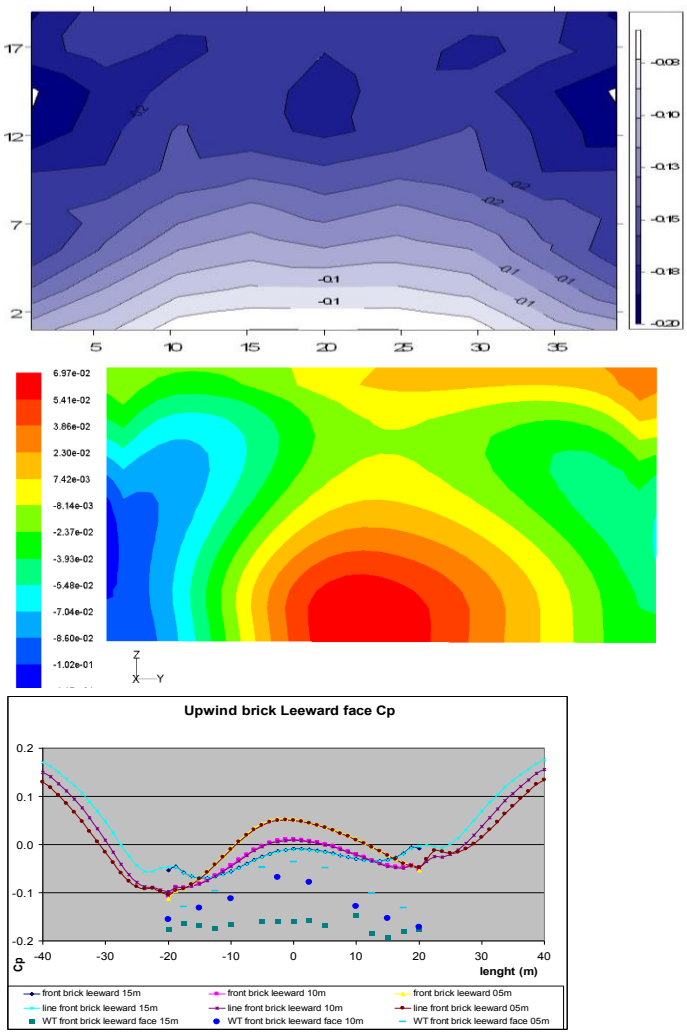

Figure 19: WT (top), CFD (middle) and Cp's contours plot and graphic (bottom) for the upwind brick leeward face at 90˚ (H/W=1.00).

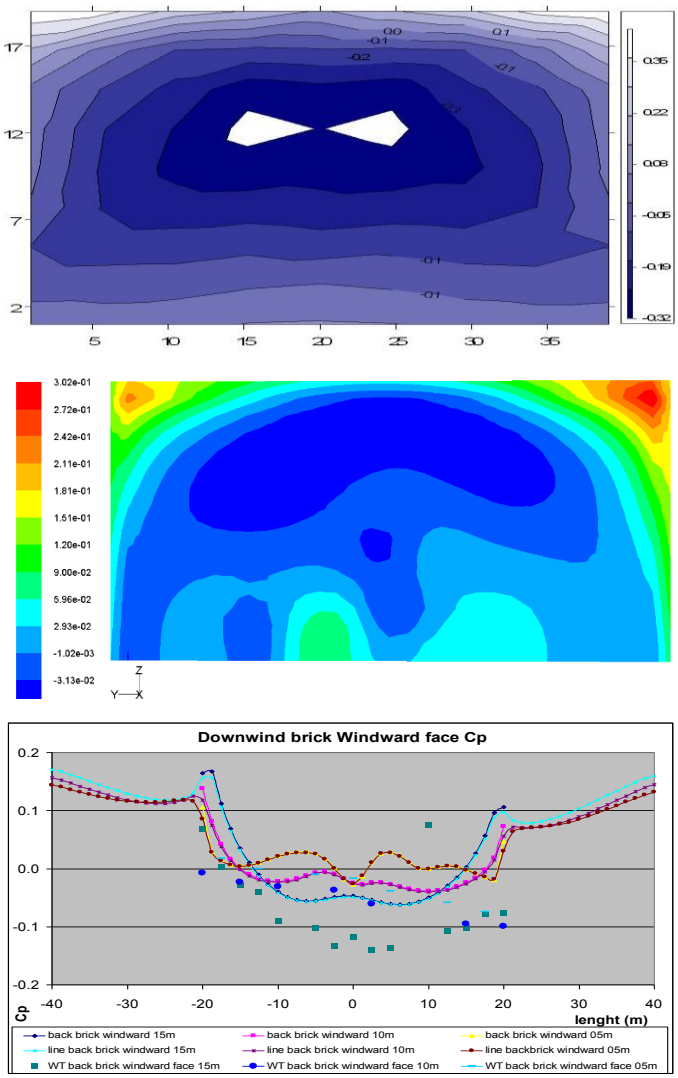

Figure 20: WT (top), CFD (middle) and Cp's contours plot and graphic (bottom) for the downwind brick windward face at 90˚ (H/W=1.00).

1. Bricks parallel to the airflow (at 0˚)

Here the pair of bricks was placed paralleled to the airflow, which corresponds to the inside face of a canyon along the mainstream. Four aspect ratios were simulated for this wind direction in WT, while the aspect ratio H/W= 1.0 was performed in both WT and CFD methods.

Similarity is observed between both the windward and the leeward side contour plots from the WT and the CFD simulations, with some low resolution on the WT image due to the few pressure taps used on the front and rear sides (Figure 21 to Figure 23). On the other hand, Cp range of results matches well, except for the lowest ones in the scale. These are lower in the CFD output due to the accuracy the software calculation can reach with a fine mesh and grid solution. Moreover, comparison among the wind tunnel outputs for all the ranges investigated (H/W= 2.00, 1.00, 0.66, and 0.50) did not show much variation on the results from the narrowest until the widest aspect ratios. The

same observations are valid for the top side, on which both the Cp results and the contour plots from the WT and the CFD are matching well.

Regarding the results for the left brick right (inside) face for the same number of simulations just quoted, it is possible to observe a close range between the WT and the CFD results for a H/W aspect ratio = 1.00. Further, a sharp drop of pressure right after the upwind vertical corner, which is clearly seen in the graphic also, is related to airflow detachment in this edge and later reattachment after 1/8 of the block length.

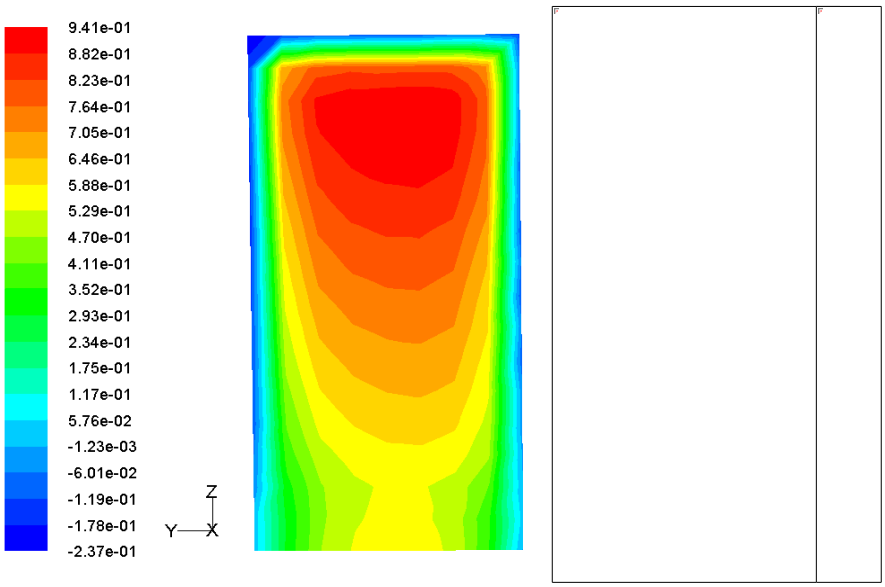

Figure 21: CFD (left) and WT (right) Cp's contour plots for the left brick windward face at 0˚ (H/W=1.0).

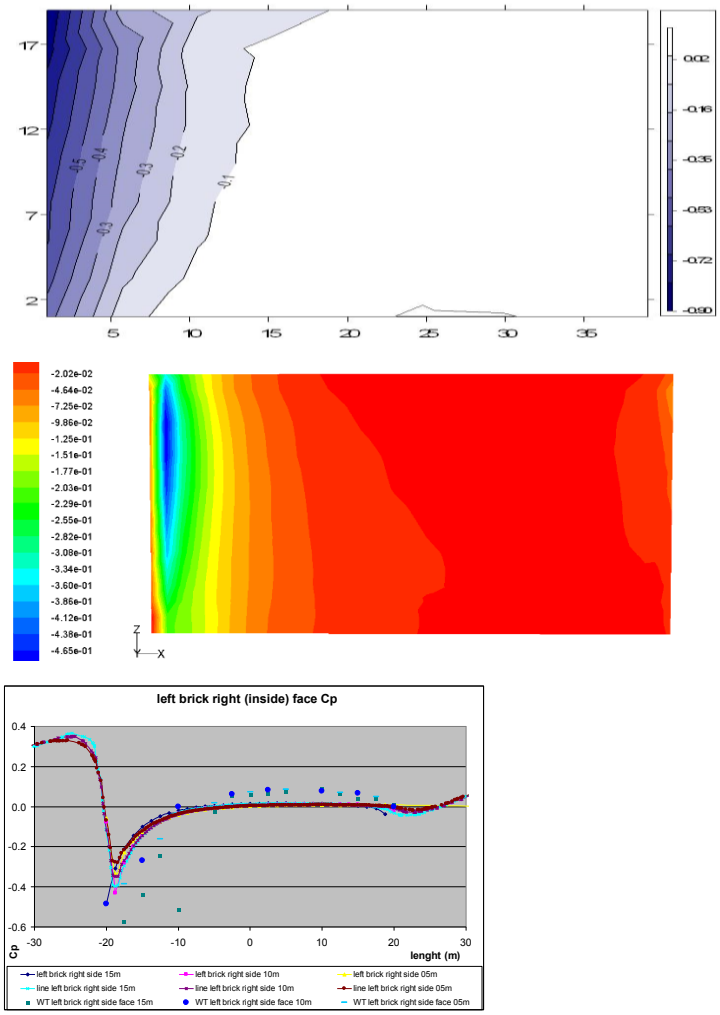

Figure 22: WT (top), CFD (middle) and Cp's contours plot and graphic (bottom) for the left brick right face at 0˚ (H/W=1.0).

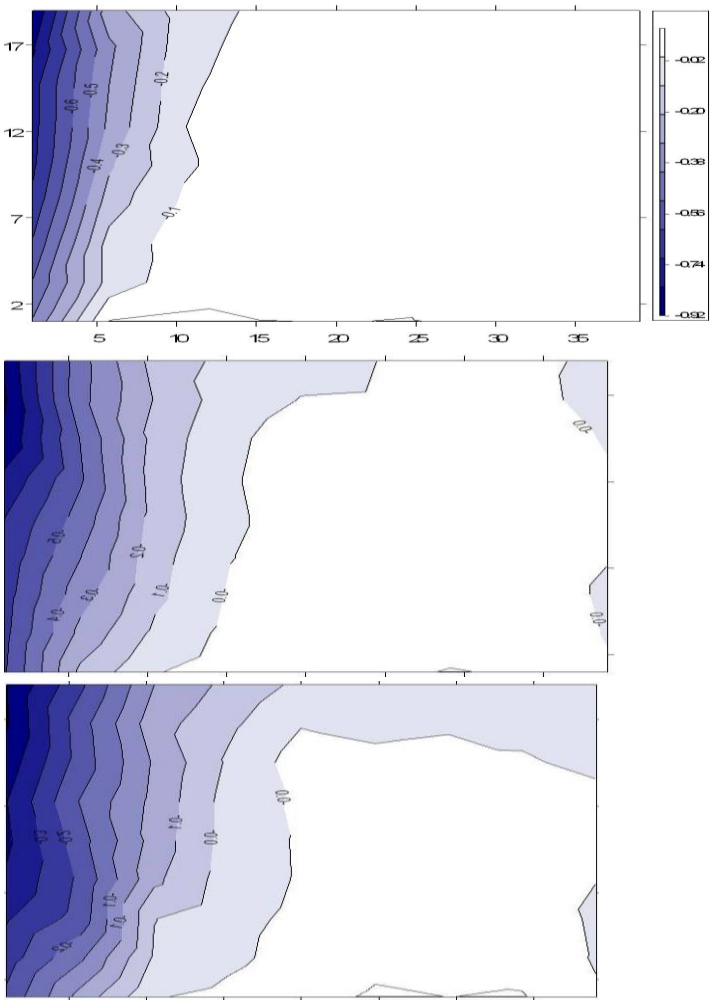

Figure 23: WT (top), CFD (middle) and Cp's contours plot and graphic (bottom) for the left brick right face at 0˚ (H/W=2.00, H/W=0.66, and H/W=0.55).

1. Bricks oblique to the airflow (at 45˚)

Here the pair of bricks was placed skewed 45˚ to the airflow. The four aspect ratios were simulated for this wind direction in the wind tunnel, while the aspect ratio H/W= 1.0 was performed in both WT and CFD methods.

From the observation of the Figure 24 to Figure 26 it is possible to affirm that reasonable equivalence was obtained between the wind tunnel and the CFD outputs on the contour plot of the top surfaces. The slanted wind at the upper edge of the brick creates a curly flow that results in a diagonal detachment flow. This happens on both the upwind and the downwind bricks since both are exposed to the open flow. Conversely, on the second half of the top surface of the downwind brick this effect is broken due to the wake interference from the first brick. This can be noticed also in the airflow visualization pathlines in the next item of analysis. Regarding the Cp values, again the CFD calculation seems to overestimate the pressure on the top surface, as was already observed in the previous analysis of the results for the other top surfaces.

Figure 24 shows results for the external side of the upwind brick for oblique winds. Although the contour plots from the WT do not mark the FS point as precisely as in the CFD, good equivalence between both for Cp results and contours was found. Figure 25 show the results for the rear side of the downwind brick. Here good similarity between the WT and the CFD results is seen as well.

Figure 26 shows results for the rear side of the upwind brick for an aspect ratio of 1.0. Good equivalence between both the WT and CFD contours plots and Cp range of results can be observed once more. When WT results for H/W= 1.0 are contrasted to the H/W at 2.0, 0.66 and 0.50 aspect ratios, it is possible to observe a quite similar range of results and overall contour patterns. On the other hand, the area of high pressure on the left side near ground increases gradually from the widest to the narrowest set of bricks. Good similarity was found also for the windward side of the downwind brick for H/W= 1.0, and its contrast to the other aspect ratios (H/W= 2.0, 0.66 and 0.50), although the high-pressure spot was found on the top right side of the surfaces

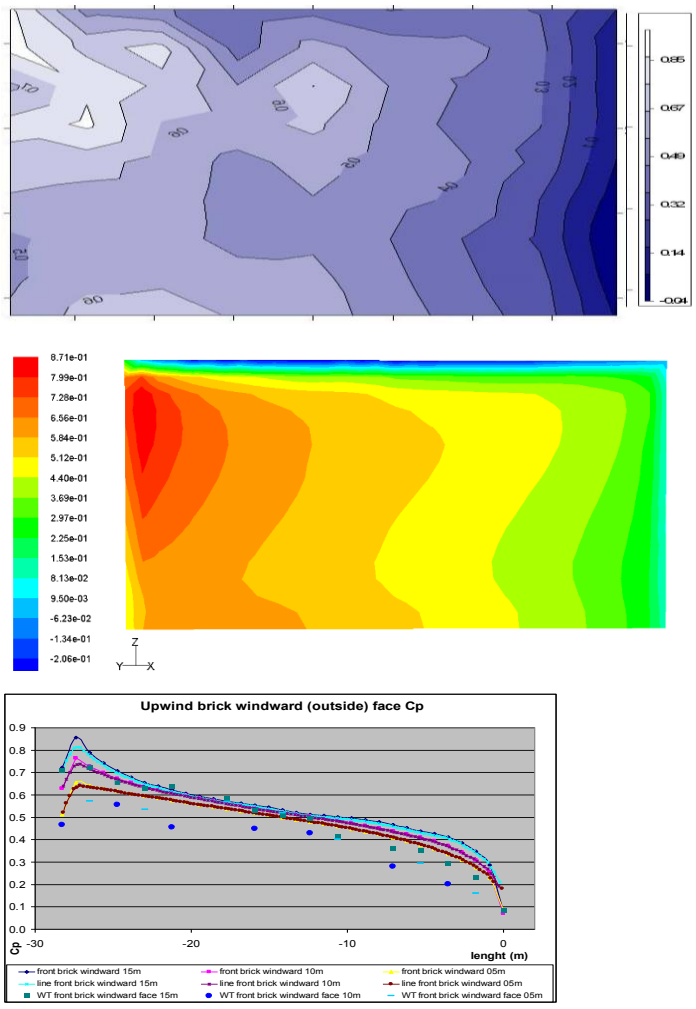

Figure 24: WT (top), CFD (middle) and Cp's contours plot and graphic (bottom) for the upwind brick windward (outside) face at 45˚ (H/W=1.0).

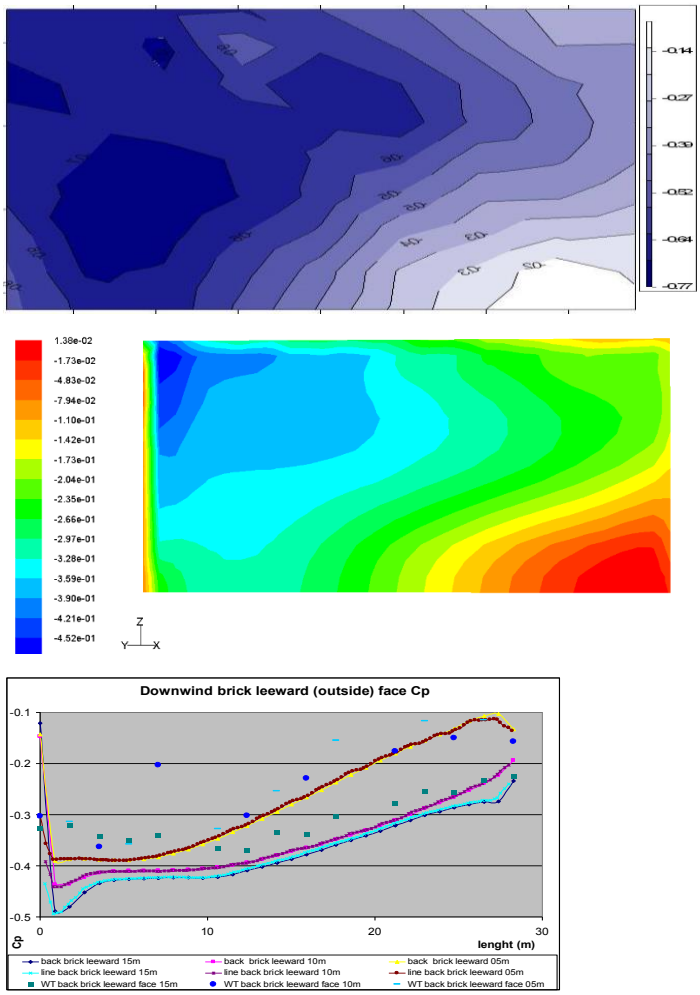

Figure 25: WT (top), CFD (middle) and Cp's contours plot and graphic (bottom) for the downwind brick leeward face at 45˚ (H/W=1.0).

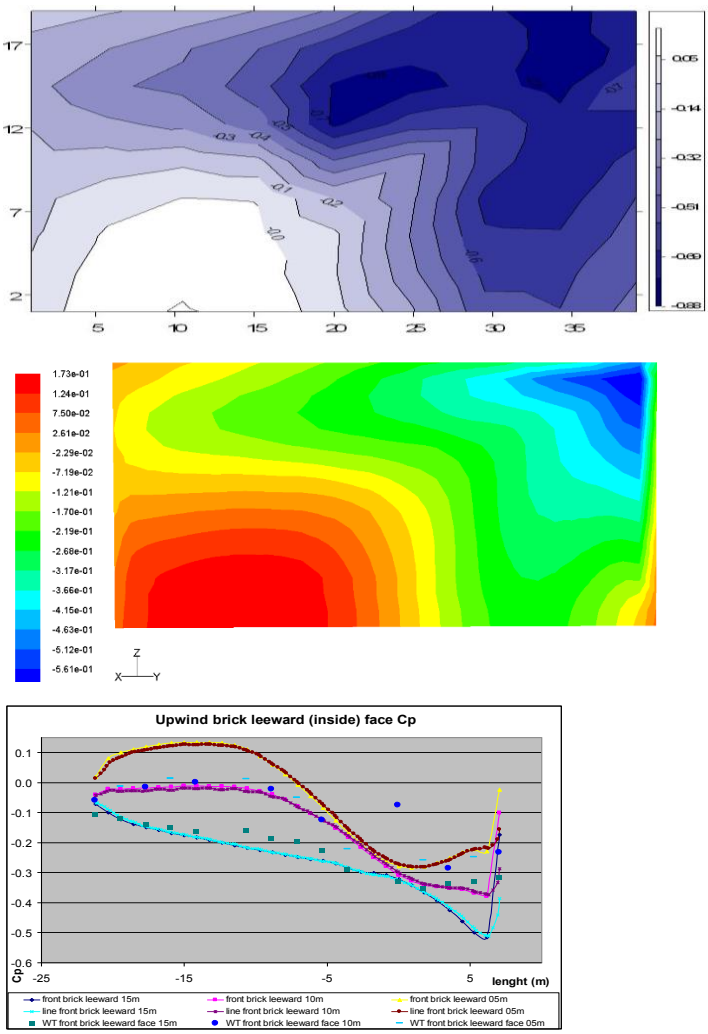

Figure 26: WT (top), CFD (middle) and Cp's contours plot and graphic (bottom) for the upwind brick leeward (inside) face at 45˚ (H/W=1.0).

1. WT and Cp average results comparison

The averaged Cp results for the windward and the leeward faces from each block and from both WT and CFD experiments were compared with results from Liddament (1996) (Table 3). The ABL achieved in the WT experiments and employed in the CFD simulations is comparable to an urban terrain wind profile. On the other hand, the reference literature presents results for three types of terrain: open field, sub-urban, and urban areas. Further, while the experiments conducted in this research refer to a set of two parallel rectangular bricks, the reference literature results are based on an isolated rectangular volume, regardless the ABL variations. Finally, not all sets of H/W bricks that were investigated in the WT were simulated on CFD.

Good agreement was found for the Cp total average results comparison for most of the scenarios. Conversely, divergent outputs were observed either between the WT and the CFD or among both and the reference literature, with consistent pattern related to either the H/W aspect ratio or the wind incidence. Strong agreement was found

between the WT and the CFD Cp average results for the windward side of the upwind brick with orthogonal and oblique prevailing winds, with values also matching with the ones for open field ABL from the reference literature. For the windward side of the downwind brick (inside the canyon) with orthogonal prevailing winds, the results agree for the 0.50 and 0.66 H/W aspect ratios, with are the widest ones. For the 1.0 and the 2.0 H/W, square and narrow canyon scenarios, the CFD results were around 0.20 greater than the WT ones. Conversely, for oblique winds the Cp results agree well between both methods of research for the 0.50, 0.66, and the 1.00 H/W scenarios, keeping the same Cp difference of 0.20 the CFD result above the WT for the 2.0 H/W narrow canyon. On the other hand, the Cp results for the leeward side, while the upwind brick leeward face from the WT and the CFD experiments were contrasted between them, the results for the downwind brick leeward face from both the WT and the CFD experiments were compared also to the single brick leeward face from the literature. Regardless the wind orientation (45º or 90º) and the brick position, it was found that the CFD Cp results overcomes the WT results by a constant 0.35 and 0.30 for the 0.50 and 0.66 H/W, and the 1.0 and 2.0 H/W aspect ratio canyons, respectively. Alternatively, the WT Cp results for the downwind brick leeward face match well with the ones from the literature for ABL urban areas. Good agreement of Cp averaged results was found for parallel winds to the set of bricks among the WT, the CFD, and the reference literature (with ABL for urban areas), although the CFD results were consistently around 0.10 greater than either one of the other sources.

Table 3: Cp results from the sets of WT and CFD experiments and found in the literature:

Cp averaged results		H/W aspect ratio								Liddament (1996)		
wind α	face	0,50		0,66		1,00		2,00		open field	sub-urban areas	urban areas
		WT	CFD	WT	CFD	WT	CFD	WT	CFD			

0˚	left brick inside	-0.19	-	-0.17	-	-0.160	-0.051	-0.16	-	-0.50	-0.35	-0.20
	left brick outside	-0.18	-	-0.17	-	-0.170	-0.046	-0.16	-	-	-	-
	right brick inside	-0.19	-	-0.15	-	-0.150	-0.045	-0.18	-	-	-	-
	right brick outside	-0.17	-	-0.17	-	-0.160	-0.049	-0.17	-	-0.50	-0.35	-0.20
45˚	front brick windward	0.43	-	0.43	-	0.43	0.540	0.43	-	0.25	0.20	0.15
	front brick leeward	-0.57	-	-0.53	-	-0.43	-0.150	-0.37	-	-	-	-
	rear brick windward	0.42	-	0.35	-	0.20	0.234	-0.03	-	-	-	-
	rear brick leeward	-0.54	-	-0.54	-	-0.54	-0.270	-0.54	-	-0.60	-0.50	-0.32
90˚	front brick windward	0.64	0.690	0.64	0.690	0.64	0.690	0.64	0.670	0.60	0.25	0.06
	front brick leeward	-0.30	0.034	-0.29	0.029	-0.33	-0.013	-0.37	-0.051	-	-	-
	rear brick windward	0.29	0.210	0.10	0.120	-0.06	0.150	-0.25	-0.034	-	-	-
	rear brick leeward	-0.34	0.067	-0.34	0.090	-0.34	0.015	-0.34	0.054	-0.70	-0.50	-0.30

Source: this research and Liddament (1996).

Visualization of airflow effects and patterns

As described in the literature review presented in the introduction section, for canyons perpendicular to the flow (at 90˚), vortexes can be observed rotating in the mainstream direction below the canopy height and between the two blocks by using helium bubbles in the wind tunnel and from CFD simulation (Figure 27 to Figure 29).

The vortex occurs as a result of pressure differences between the leeward side of the upstream building (low pressure) and the windward side of the downstream building (high pressure). The pressure difference rises when the free airflow creates an increase in the pressure on the windward surface of the front block and forces a down flow below the frontal stagnation point. The flow separates at the edge of the leeward surface, creating a large wake of low pressure behind the front block. When the detached flow meets the windward surface of the rear block, it tends to

be diverted downward, which increases the pressure on the latter block's surface. When, on reaching ground level, the flow turns towards the low-pressure area on the leeward side of the frontal block, it gives rise to a flow across the canyon and in a direction reverse to that of the mainstream. From this point the flow is diverted upwards due to its mass conservation and rises, though with a weaker vertical component. When reaching the top edge, where a strong flow detachment takes place, this flow is deflected into the horizontal wind stream direction again. The vortex created in the canyon space therefore presents wind components near the surfaces but little air movement at its centre.

The flow visualization and vortices observed in Figure 27 to Figure 29 agree with description in the literature (Chang et al 1971; DePaul and Shieh 1986; Oke 1988 Hunter et al., 1991; Sini et al., 1996). The production of flow effects and vortices vary according with the canyon's H/W aspect ratios, with skimming flow being observed for the narrow canyons (aspect ratio H/W=2.0) (Figure 27), isolated roughness flow being observed for the canyons with square cross-section (aspect ratio H/W=1.0) (Figure 28), and with wake interference flow happening in wide canyons (aspect ratio H/W=0.5) (Figure 29), with good agreement being observed between the visualization from the tests in the wind tunnel and from the calculated results from the CFD simulation

Bricks H/W aspect ratio of 2.00

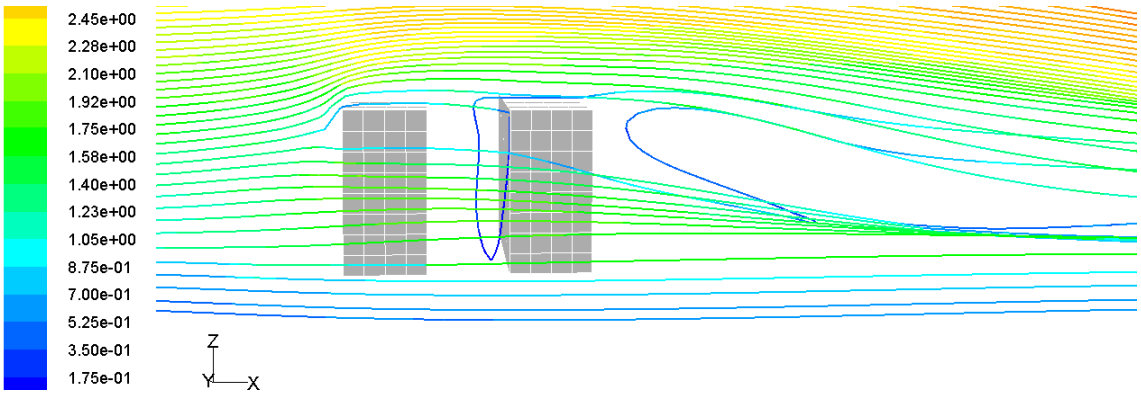

(a)

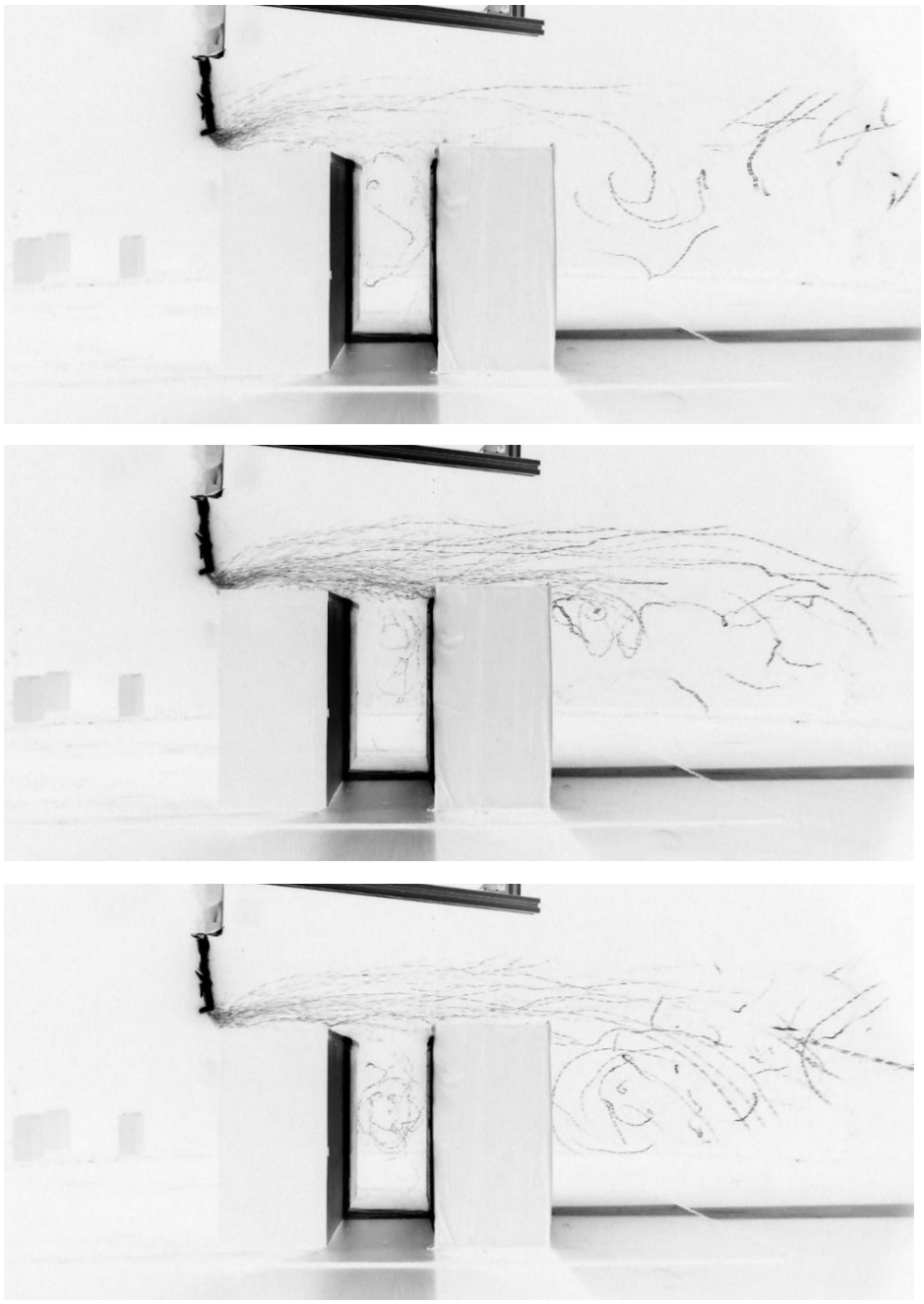

(b)

Figure 27: Velocity magnitude pathlines view and sequence of airflow visualization by using helium bubbles in the wind tunnel (a) and from CFD simulation (b) (90˚; H/W=2.0).
Bricks H/W aspect ratio of 1.00

(a)

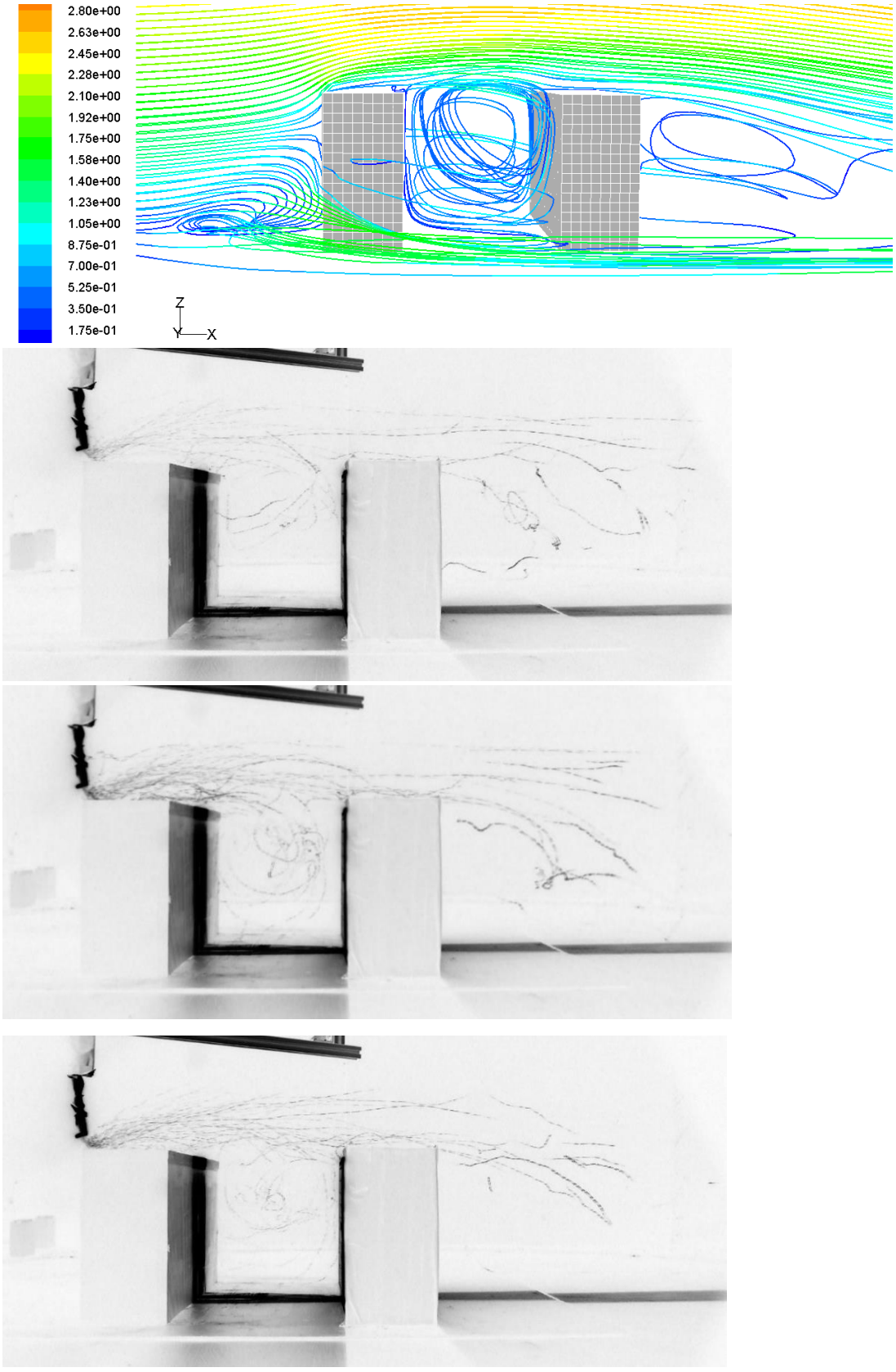
2.80e+00
2.63e+00
2.45e+00
2.28e+00
2.10e+00
1.92e+00
1.75e+00
1.58e+00
1.40e+00
1.23e+00
1.05e+00
8.75e-01
7.00e-01
5.25e-01
3.50e-01
1.75e-01
Z
Y
X

(b)

Figure 28: Sequence of airflow visualization by using helium bubbles in the wind tunnel (a) and from CFD simulation (b) (90˚; H/W=1.0).

Bricks H/W aspect ratio of 0.50

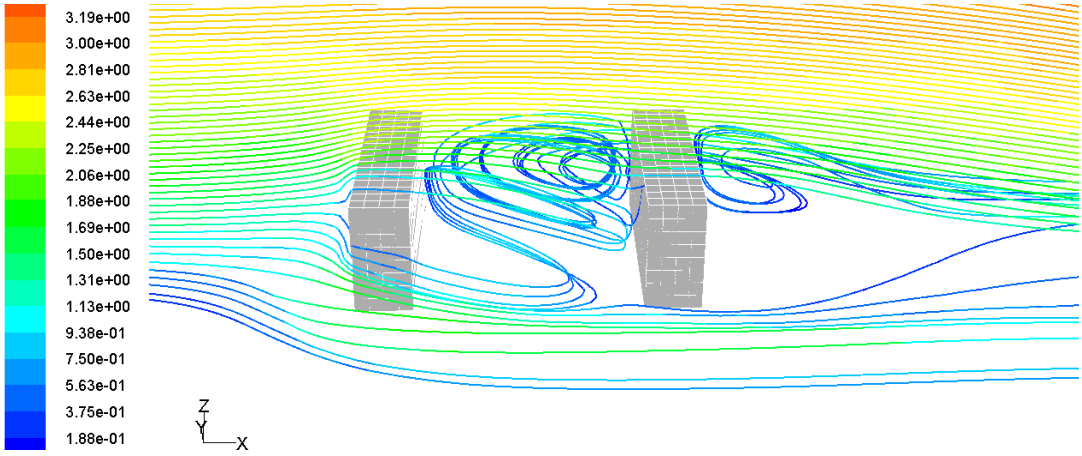

(a)

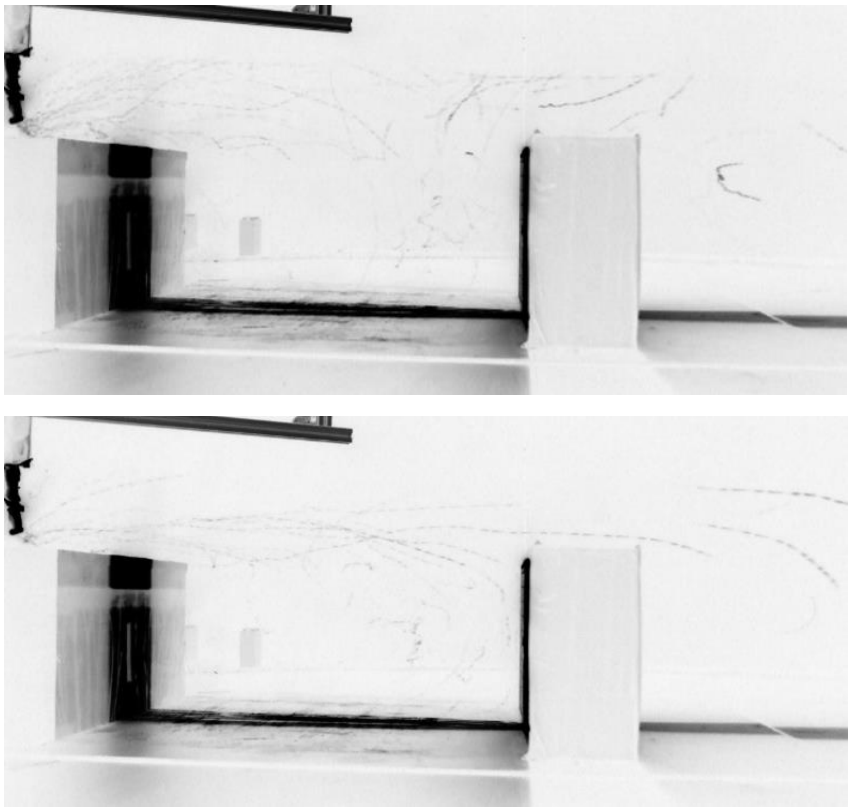

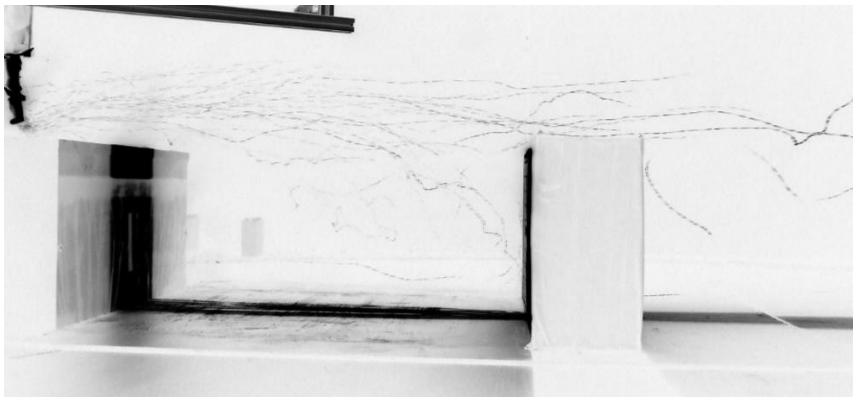

(b)

Figure 29: Sequence of airflow visualization by using helium bubbles in the wind tunnel (a) and from CFD simulation (b) (90˚; H/W=0.50).

Assessment of the wind profile

The velocity magnitude from the CFD outputs was assessed on each model by 15 vertical lines strategically positioned near the walls and inside the canyon, in contrast with the free ABL profile. The analysis was carried out for the three wind directions on the H/W=1.0 canyon (Figure 30); and for the orthogonal flow for four H/W ratios (Figure 31).

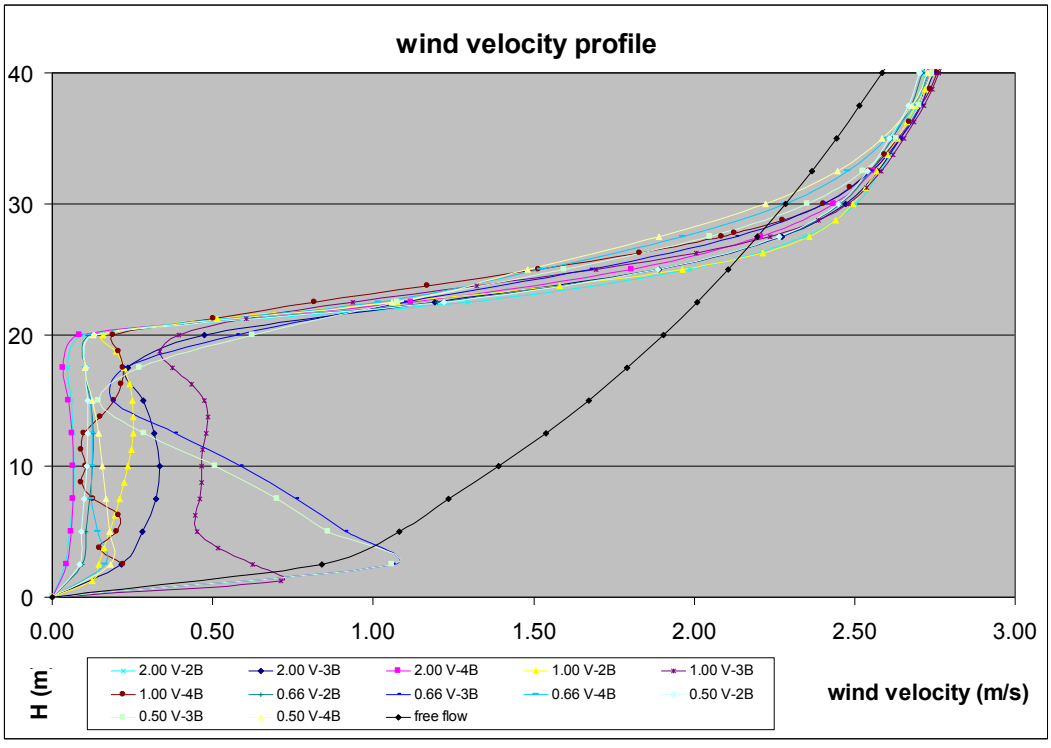

Figure 30: wind profile across the canyon for all H/W ratios (90˚; m/s).

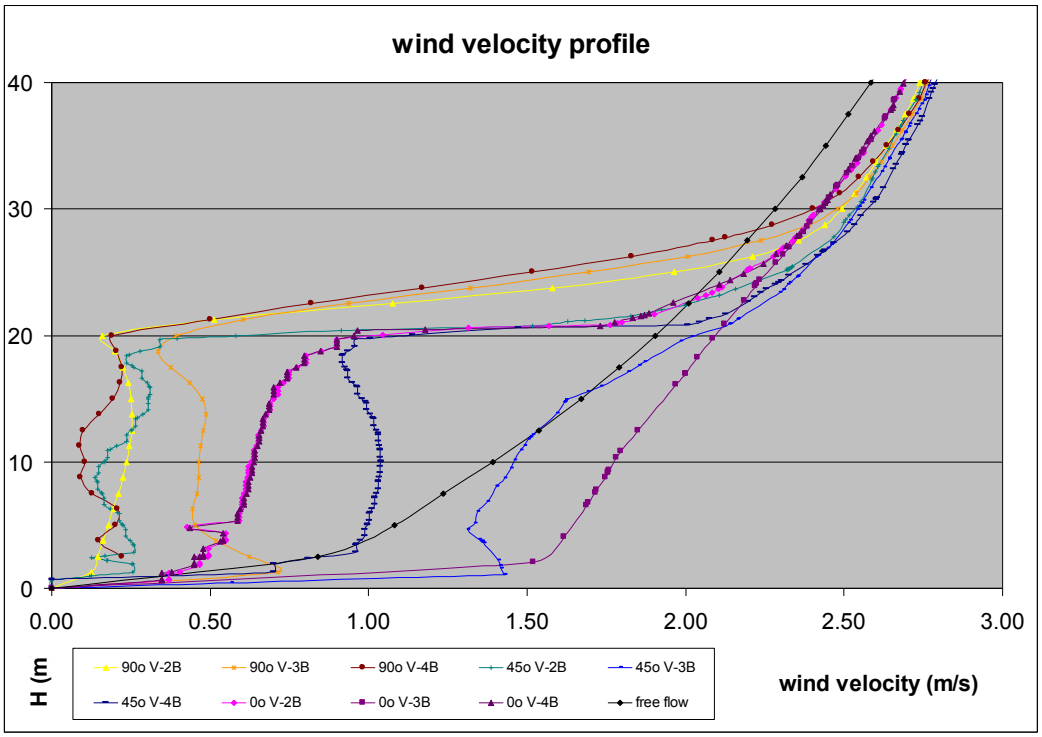

Figure 31: wind profile across the canyon for all wind directions (H/W= 1.0; m/s).

By assessing the wind profiles in the central axis of these canyons it is possible to affirm that the wind velocity around 5m height right in it centre (V-3B), when contrasted to the one found in the free airflow at the same height, has the following influence of the canyon shape: the narrowest set with H/W=2.0 shows reduction of 65%; the square set with H/W=1.0 has a reduction of 25%; and both the H/W of 0.66 and 0.50 present increase of 25%. This happens due to the skimming flow effect in the first case and wake interference flow in the last two cases. These effects were also highlighted in the airflow visualization analysis and agree with the statement made about the airflow effects inside canyons in the previous paragraph. It is possible to say that most of the wind profiles presented show decrease of air velocity inside the canyon. Conversely, the slanted winds present less decrease of velocity when compared to the orthogonal and parallel ones. At 05m height this decrease ranges from 50% to 80% of the free flow wind profile. The exceptions are the profiles in the centre of the canyon for both the skewed 45˚ flow and alongside the bricks (0˚) flows, which show increases of velocity of 20% and 60%, respectively. These accelerations occur due to the vortex created after the bouncing of the flow on the windward side of the downwind brick in the first case and the Venturi acceleration effect in the second one.

Conclusion

Simulation of the airflow field around several sets of two parallel bricks was performed for three wind directions on both wind tunnel and CFD calculation.

The CFD simulations were able to reproduce the main features of the airflow effectively. This was demonstrated by the assessment of numerical and visual results. For instance, pressure coefficient contour plots with comparable shape and numerical results were achieved between both methods of simulation.

It was also highlighted the limitations of the CFD solver adopted in reproducing accurate flow detachments and wake reattachment, although similar airflow patterns were identified for the same set of aspect ratios on both the wind tunnel helium bubble visualization and the CFD airflow visualization by vectors and pathlines.

In addition, the CFD software allows identifying velocity, pressure and turbulence profiles in any direction and region of the model, allowing a more complex and accurate assessment of the problem.

Concluding, the comparison of the CFD output matched well with the results from the wind tunnel. Therefore, this research calibrates the parameters adopted on the pre-processing, the solving and the post-processing stages of the computational models.

Repository

The complete results shown in this paper can be accessed in an appendix document available via the google-drive link: https://drive.google.com/drive/folders/1D-dsJyPTY2bZhD6AIaeHy2OeztA8CKKd?usp=sharing

Acknowledgements

The author would like to express his gratitude the Welsh School of Architecture at Cardiff University, were this PhD research was carried out, and respectively to Professor Phil Jones and Dr Don Alexander, from the Welsh School of Architecture at Cardiff University, the first and the second supervisors. Further acknowledgements of gratitude are extended to the Research Assistant Dylan Dixon and the WSA staff Huw Jenkins, Yan Wang, and Simon Lannon, for their essential support for the accomplishment of this research.

References

1. Givoni, B. 1991. Impact of planted areas on urban environmental quality: A review. Atmospheric Environment 25B(3), pp. 289-299.
2. Givoni, B. 1993. Semiempirical model of a building with a passive evaporative cool tower. Solar Energy 50(5), pp. 425-434.
3. Givoni, B. 1994. Passive and Low Energy Cooling of Buildings. New York: John Wiley & Sons.
4. Givoni, B. 1998a. Climate Considerations in Building and Urban Design. New York: Van Nostrand Reinhold.
5. Givoni, B. 1998b. Effectiveness of mass and night ventilation in lowering the indoor daytime temperatures. Part I: 1993 experimental periods. Energy and Buildings 28, pp. 25-32.
6. Melaragno, M. G. 1982. Wind in Architectural and Environmental Design. New York: Van Nostrand Reinhold.
7. MacDonald, A. J. 1975. Wind Loading on Building. London: Applied Science Publisher.
8. Oke, T. R. 1978. Boundary Layer Climates. London: Methuen & Co.
9. Oke, T. R. 1988. Street design and urban canopy layer climate. Energy and Buildings 11, pp. 103-113.
10. Oke, T. R. 1973. City size and the urban heat island. Atmospheric Environment 7(8), pp. 769-779.
11. Cook, N. J. 1985. Designer's Guide to Wind Loading of Building Structures. London: Butterworths.
12. Holmes, J. D. 2001. Wind Loading of Structures. New York: Spon Press.
13. Kolokotroni, M. and Santamouris, M. 2007. Ventilation for cooling. In: Santamouris, M. ed. Advances in Passive Cooling. London: Earthscan, pp. 140-189.
14. Masi, M. and Ochoa, A. Il Vento. Climatizzazione Naturale degli Edifici e Impianti a Energia Pulita. Roma: DEI Tipografia del Genio Civile.
15. Plate, E. and Kiefer, H. 2001. Wind loads in urban areas. Journal of Wind Engineering and Industrial Aerodynamics 89, pp. 1233–1256.
16. CIBSE A. 2010. Environmental Design: CIBSE Guide A. Chartered Institution of Building Services Engineers. 7 ed. London: CIBSE.
17. Awbi, H. B. 1998a. Calculation of convective heat transfer coefficients of room surfaces for natural convection. Energy and Buildings 28, pp. 219-227.
18. Awbi, H. B. 1998b. Chapter 7 – Ventilation. Renewable and Sustainable Energy Reviews 2, pp. 157-188.
19. Awbi, H. B. 1991. Ventilation of Buildings. London: E & FN Spon.
20. Awbi, H. B. 2003. Ventilation of Buildings. 2 ed. London: Spon Press.
21. Olgyay, V. 1963. Design with Climate. Princeton: Princeton University Press.
22. Olgyay, V. 1973. Design with Climate. Bioclimatic Approach to Architectural Regionalism. New Jersey: Princeton University Press.
23. Chegung, J. C. K. 1984. Effect of tall building edge configurations on local surface wind pressures. In: 3rd International Conference on Tall Buildings. Hong Kong and Guangzhou, 10-15 December.

24. Chandra, S. et al. 1986. Cooling with Ventilation. A Product of the Solar Technical Information Program Published by Solar Energy Research Institute, Operated for the U.S. Department of Energy. Cocoa, Florida: Florida Solar Energy Center.
25. Vardoulakis, B. et al. 2003. Modelling air quality in street canyons: a review. Atmospheric Environment 37 (2), pp. 155-182.
26. Nakamura, Y. Oke, T. R. 1988. Wind, temperature and stability conditions in an east-west oriented urban canyon. Atmospheric Environment 22(12), pp. 2691-2700.
27. Johnson, G. T. and Hunter, L. L. 1998. Urban wind flows: Wind tunnel and numerical simulations — A preliminary comparison. Environmental Modelling & Software 13, pp. 279–286.
28. Johnson, G. T. and Hunter, L. J. 1999. Some insights into typical urban canyon airflows. Atmospheric Environment 33, pp. 3991-3999.
29. Hunter, L. J., Watson, I. D. and Johnson, G.T. (1991) Modelling air flow regimes in urban canyons. Energy and Buildings 15-16, pp. 315-324.
30. Wedding, J. B. et al. 1977. A wind tunnel study of gaseous pollutants in city street canyons. Journal of Air Pollution Control Association 27, pp. 557-566.
31. Arnfield, A. J. and Mills, G. 1994. An analysis of the circulation characteristics and energy budget of a dry, asymmetric, east, west urban canyon. I. Circulation characteristics. International Journal of Climatology 14, pp. 119-134.
32. Santamouris M, et. Al. 1999. Thermal and airflow characteristics in a deep pedestrian canyon under hot weather conditions. Atmospheric Environment. 33, pp. 4503-4521.
33. Georgakis, Ch. and Santamouris, M. 2004. On the air flow in urban canyons for ventilation purposes. The International Journal of Ventilation 3(1), pp. 53-66.
34. Georgakis C. and Santamouris, M. 2005. Wind and Temperature in the Urban Environment. In: Ghiaus, C.; Allard, F. Natural Ventilation in the Urban Environment: Assessment and Design. URBVENT. London: Earthscan, pp. 81-102.
35. Chang, P. C. et al. 1971. Turbulent diffusion in a city street. In: Proceedings of the Symposium on Air Pollution and Turbulent Diffusion. Las Cruces, New Mexico, 7-10 December, pp. 137-144.
36. DePaul, F. T. and Sheih, C. M. 1986. Measurements of wind velocities in a street canyon. Atmospheric Environment 20, pp. 445-459.
37. Sini, J.-F. et al. 1996. Pollutant dispersion and thermal effects in urban street canyons. Atmospheric Environment 30, pp. 2659–2677.
38. Hoydysh, W. G. and Dabberdt, W. F. 1988. Kinematics and dispersion characteristics of flows in asymmetric street canyons. Atmospheric Environment 22, pp. 2677-2689.
39. Yamartino, R. J. and Wiegang, G. 1986. Development and evaluation of simple models for the flow, turbulence and pollutant concentration fields whitin an urban street canyon. Atmospheric Environment 20(11), pp. 2137-2156.
40. DePaul, F.S.C. 1986. Measurements of wind velocities in a street canyon, Atmospheric Environment 20, pp. 455–459.
41. Plate, E. J. 1999. Methods of investigating urban wind fields-physical models. Atmospheric Environment 33, pp. 3981-3989.

42. Cook, N. J. 1977/1978. Determination of the model scale factor in wind-tunnel simulations of the adiabatic atmospheric boundary layer. Journal of Industrial Aerodynamics 2, pp. 311-321.
43. Armitt, J. and Counihan, J. 1968. The simulation of the atmospheric boundary layer in a wind tunnel. Atmospheric Environment 2, pp. 49-71.
44. Ahmad, M. et al. 2005. Wind tunnel simulation studies on dispersion at urban street canyons and intersections – A review. Journal of Wind Engineering and Industrial Aerodynamics 93 (September), pp. 697-717.
45. Kastner-Klein, P. and Plate, E. J. 1999. Wind-tunnel study of concentration fields in street canyons. Atmospheric Environment 33, pp. 3973-3979.
46. Summers, D. M. et al. 1986. Validation of a computer simulation of wind flow over a building model. Building and Environment 21(2), pp. 97-111.
47. Davidson, M. J. et al. 1996. Wind tunnel simulations of plume dispersion through groups of obstacles. Atmospheric Environment 30 (22), pp. 3715-3731.
48. Beranek, W. J. and van Koten, H. 1979. Visual techniques for the determination of wind environment. Journal of Wind Engineering and Industrial Aerodynamics 4(3-4), pp. 295-306.
49. Jones, P. J. et al. 2004. Pedestrian wind environment around high-rise residential buildings in Hong-kong. Indoor and Built Environment. 13, pp. 259-269.
50. Elman, H. et al. 2005. Finite Elements and Fast Iterative Solvers with Applications in Incompressible Fluid Dynamics. Series Numerical Mathematics and Scientific Computation. Oxford: Oxford Science Publications.
51. Senthooran, S. et al. 2004. A computational model to calculate the flow-induced pressure fluctuations on buildings. Journal of Wind Engineering and Industrial Aerodynamics 92, pp. 1131–1145.
52. Franke, J et al. 2007. Best practice guideline for the CFD simulation of flows in the urban environment. COST Action 732, Quality Assurance and Improvement of Microscale Meteorological Models.
53. Coleman, H. W. and Stern, F. 1997. Uncertainties in CFD code validation. ASME Journal of Fluids Engineering 119, pp. 795-803.
54. Dixon, N. S. et al. 2006. Evaluation of a turbulent flow and dispersion model in a typical street canyon in York, UK. Atmospheric Environment 40, pp. 958–972
55. Caretto, L. S., et al. 1972. Two calculation procedures for steady, three-dimensional flows with recirculation. In: Proceedings of the Third International Conference in Numerical Methods in Fluid Dynamics. Paris, 3-7 July.
56. Meroney, R. N. et al. 1999. Wind-tunnel and numerical modelling of flow and dispersion about several building shapes. Journal of Wind Engineering and Industrial Aerodynamics 81, pp. 333-345.
57. Jeong, S. and Andrews, M. 2002. Application of the k–e turbulence model to the high Reynolds number skimming flow field of an urban street canyon. Atmospheric Environment 36, pp. 1137–1145.
58. De Faria, L. 2008. Airflow effects in urban canyons. In: Research Student Conference Day. The Welsh School of Architecture. Cardiff, 05 November.
59. Liddament, M. W. 1996. A Guide to Energy Efficient Ventilation. AIVC. Coventry: Oscar Faber.